POLITECNICO DI MILANO

MEMS modelling and design group

Centre for Computational Structural and Materials Mechanics

Micromechanical modeling of brittle polycrystalline films

Stefano Mariani, ***A. Ghisi, R. Mirzazadeh***

[M. Beghi, M. Bruggi, F. Confalonieri, A. Corigliano, M. Dossi, R. Martini]

ISD INSTITUT FÜR STATIK UND DYNAMIK

ISFH

Impact of mechanical and thermal load on the long term stability of PV modules

Politecnico di Milano

Department of Civil and Environmental Engineering

ENGINEERING MOTIVATION:
failure of POLYSILICON (thin) films exposed to mechanical and thermal loads

Due to mechanical and thermal loads, (thin) Si films can break because of the propagation of inter- and/or trans-granular cracks

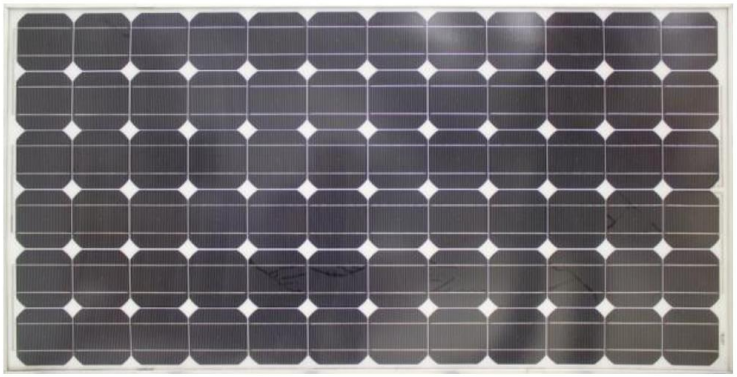

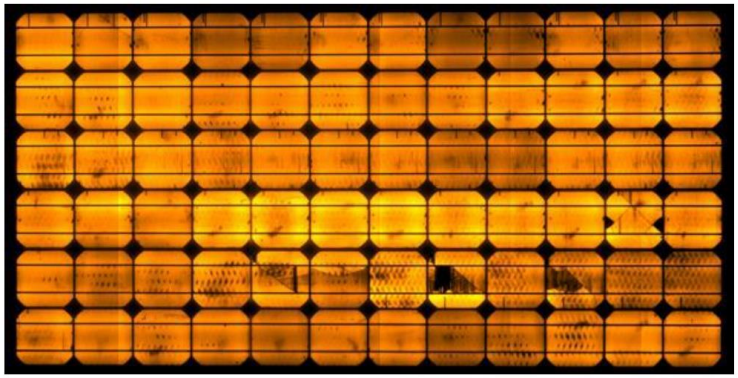

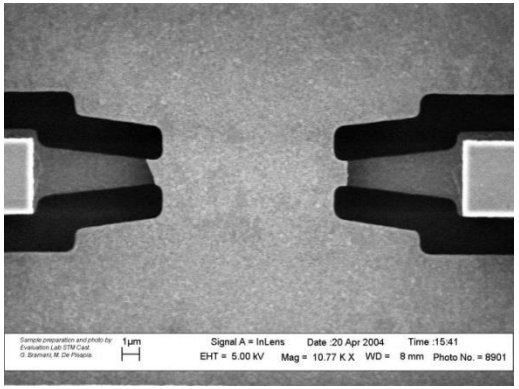

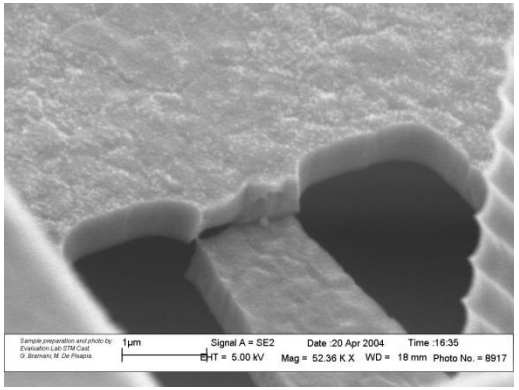

Microsystems fabrication

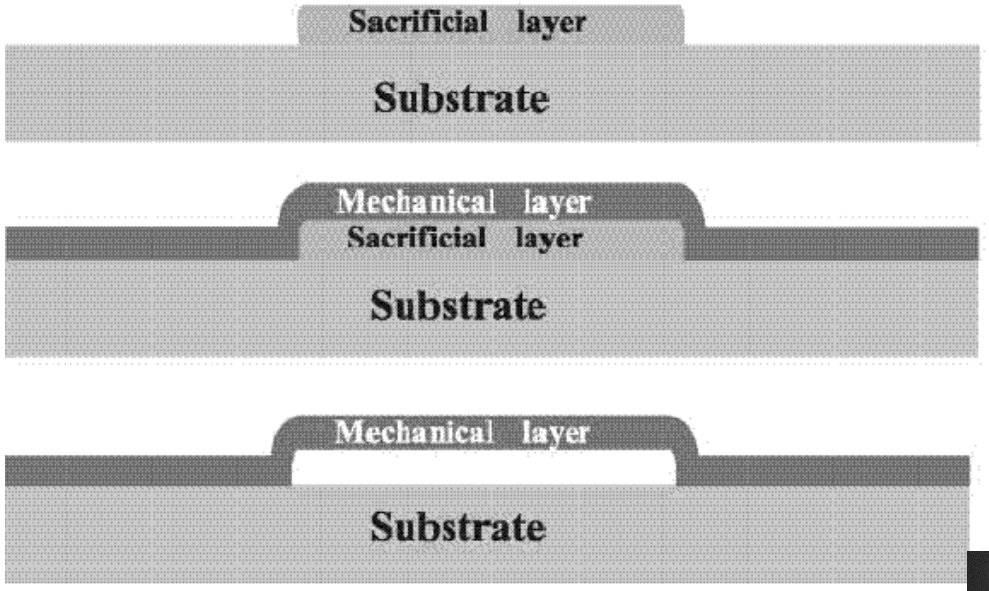

deposition of the oxide sacrificial layer

deposition of the silicon structural layer

oxide Removal

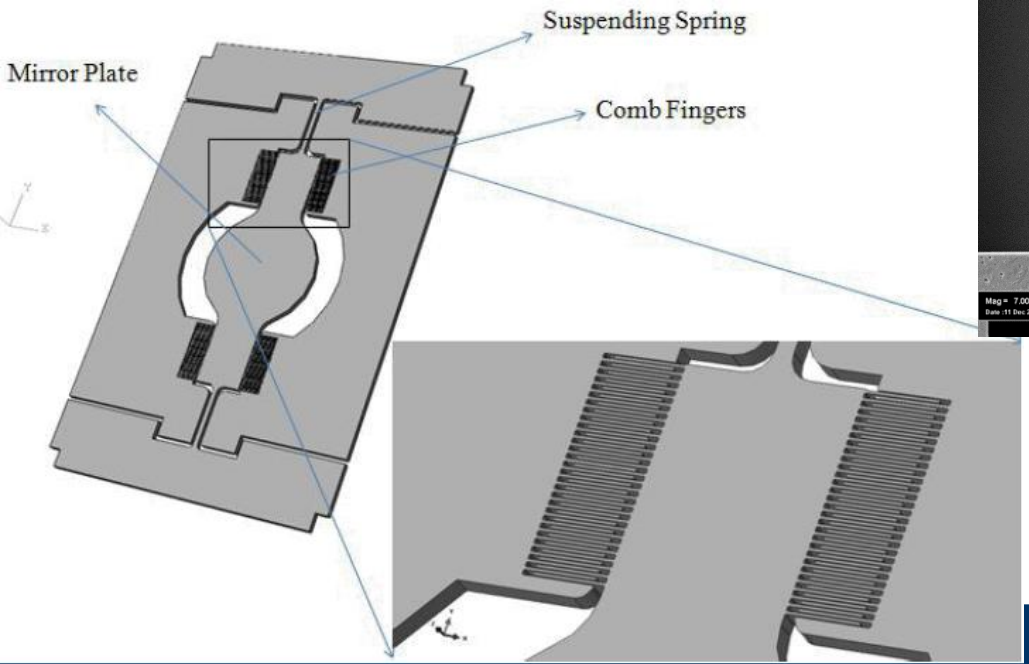

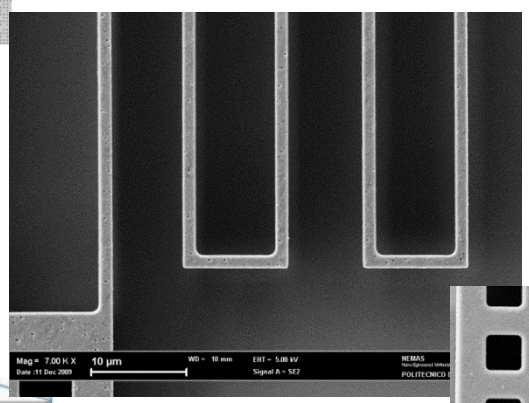

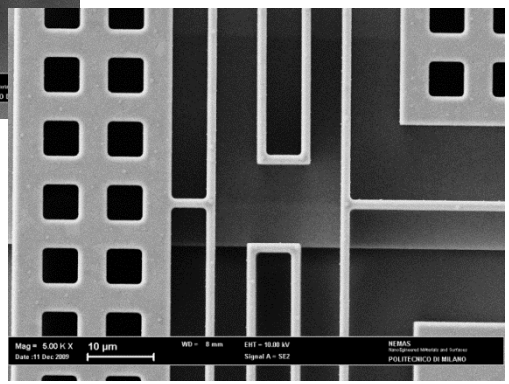

Length-scales in MEMS: from package to thin film mech.

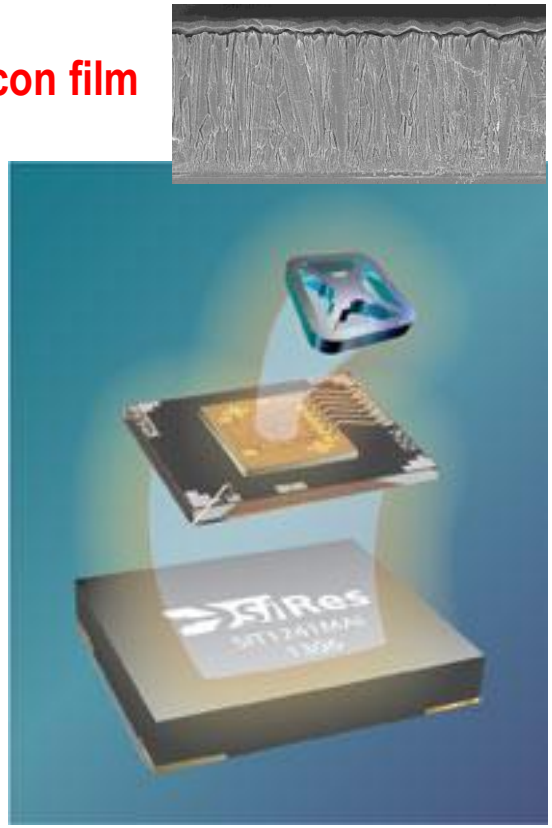

Multi-scale analysis of MEMS subject to mechanical shocks:

- decoupling between macro-scale and meso-scale allowed by small inertia of the sensor
- decoupling between meso-scale and micro-scale? (not allowed if nonlinear effects to be simulated)

	mass (Kg)
Package	$5 \cdot 10^{-4}$
Die	$2.3 \cdot 10^{-6}$
Sensor	$3 \cdot 10^{-9}$

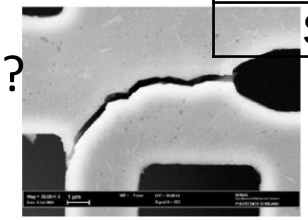

Multi-scale analysis of failure of polysilicon thin films in MEMS inertial sensors

Two-scales

Industry-oriented approach for design and testing

macro

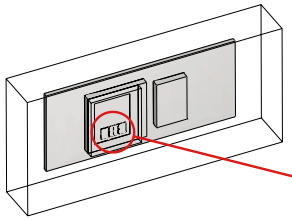

meso

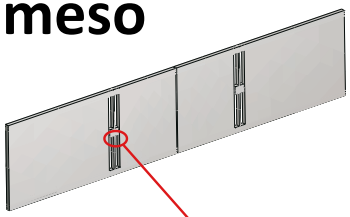

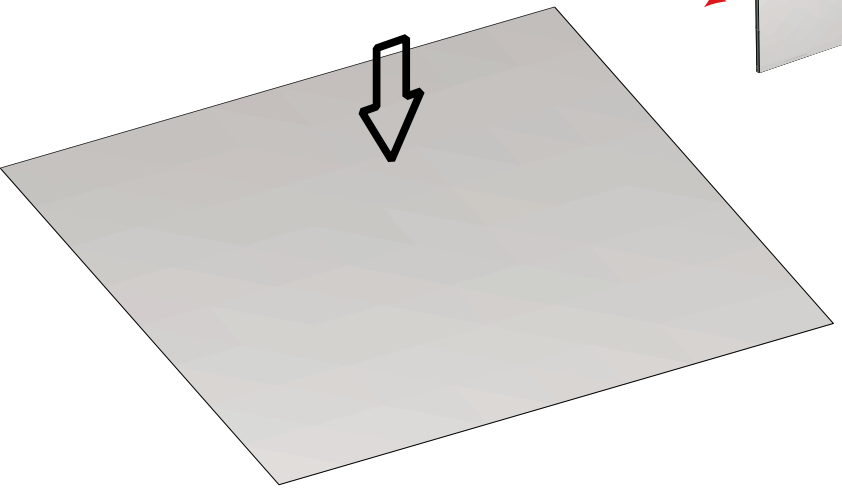

micro

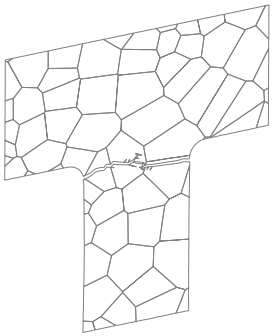

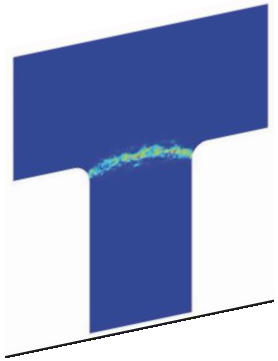

[Simplified] top-down approach

Three-scales

Understanding the underlying failure mechanisms

Multi-scale analysis (2S vs 3S) of drop and shock effects

MACRO-SCALE simulations:
effect of drop features (drop height, falling orientation) on acceleration/displacement histories at anchors.
Tool: commercial FE code

MESO-SCALE simulations:
link between drop features (drop height, falling orientation) and sensor failure probability. In 3S analyses, localization of most stressed sensor regions and input definition for micro-scale analysis.
Tool: commercial FE code + material **failure criterion**

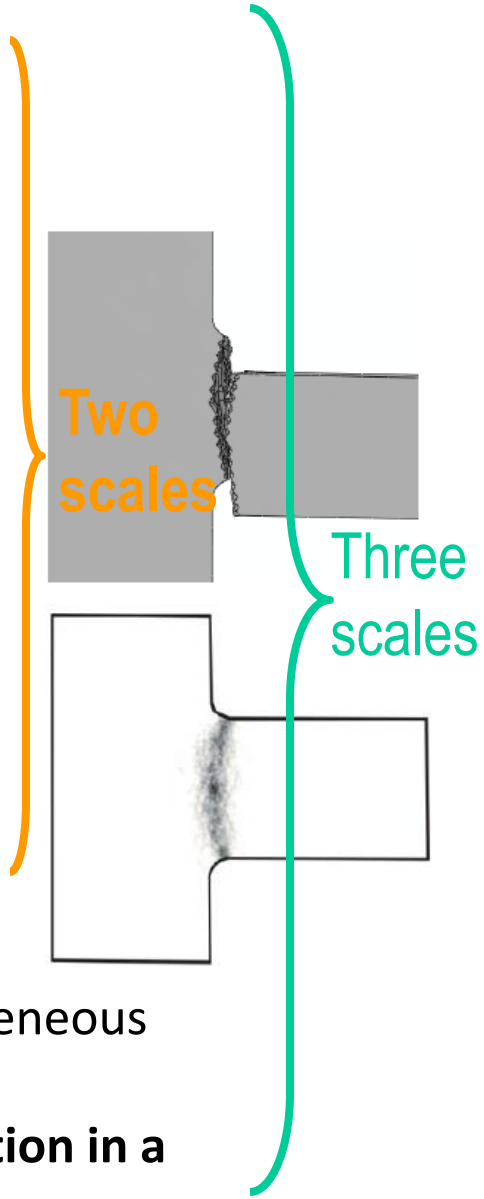

MICRO-SCALE simulations:
influence of the microstructure on failure mechanisms, heterogeneous (polycrystalline) material.
Tool: research code to **simulate fracture initiation and propagation in a polycrystal**, **Monte Carlo** simulations

On-chip testing (crack and fatigue)

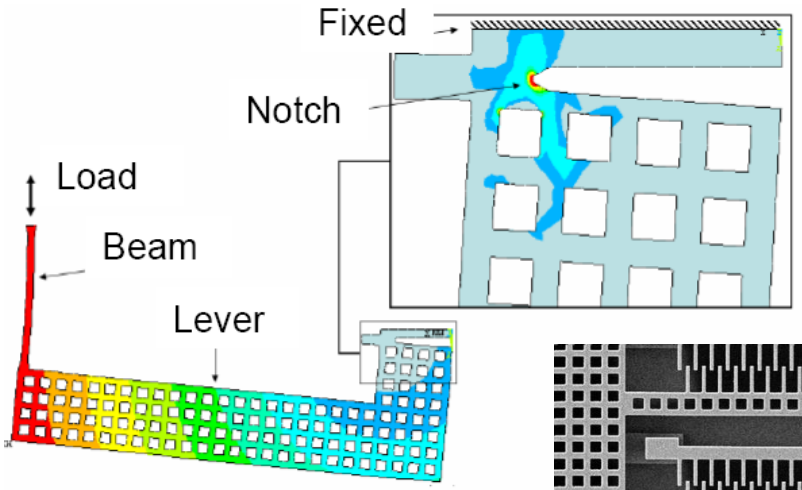

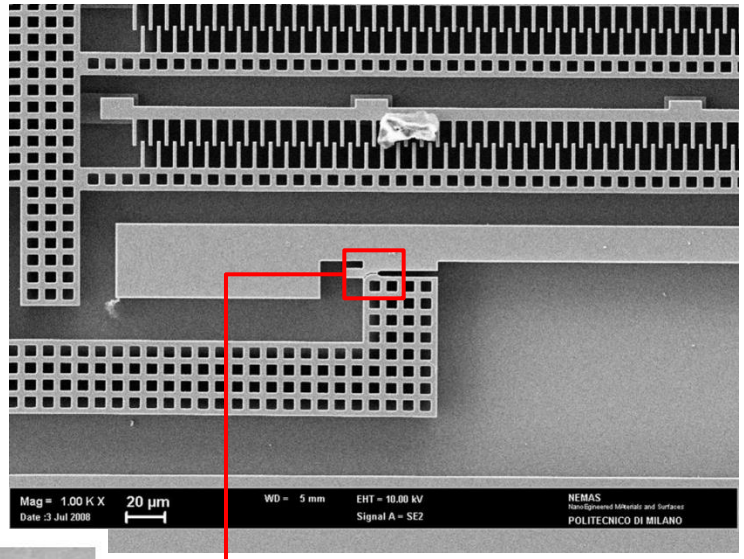

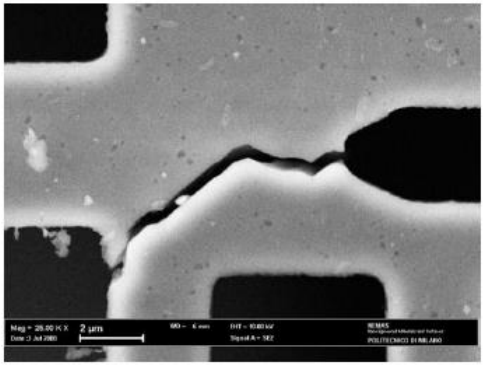

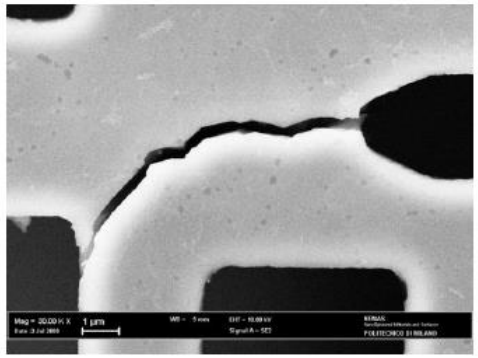

References

1. S. Mariani, A. Ghisi, A. Corigliano, S. Zerbini. Multi-scale analysis of MEMS sensors subject to drop impacts. *Sensors*, **7**, pp. 1817-1833, 2007.
2. S. Mariani, A. Ghisi, F. Fachin, F. Cacchione, A. Corigliano, S. Zerbini. A three-scale FE approach to reliability analysis of MEMS sensors subject to impacts. *Meccanica*, **43**, pp. 469-483, 2008.
3. A. Ghisi, F. Fachin, S. Mariani, S. Zerbini. Multi-scale analysis of polysilicon MEMS sensors subject to accidental drops: Effect of packaging. *Microelectronics Reliability*, **49**, pp. 340-349, 2009.
4. S. Mariani, A. Ghisi, A. Corigliano, S. Zerbini. Modeling impact-induced failure of polysilicon MEMS: a multi-scale approach. *Sensors*, **9**, pp. 556-567, 2009.
5. S. Mariani, R. Martini, A. Ghisi, A. Corigliano, B. Simoni. Monte Carlo simulation of micro-cracking in polysilicon MEMS exposed to shocks. *International Journal of Fracture,* **167**, pp. 83-101, 2011.
6. A. Ghisi, S. Kalicinski, S. Mariani, I. De Wolf, A. Corigliano. Polysilicon MEMS accelerometers exposed to shocks: numerical-experimental investigation. *Journal of Micromechanics and Microengineering*, **19**, 035023, 2009.
7. S. Mariani, A. Ghisi, A. Corigliano, R. Martini, B. Simoni. Two-scale simulation of drop-induced failure of polysilicon MEMS sensors. *Sensors*, **11**, pp. 4972-4989, 2011.
8. A. Ghisi, S. Mariani, A. Corigliano, S. Zerbini. Physically-based reduced order modelling of a uni-axial polysilicon MEMS accelerometer. *Sensors*, **12**, pp. 13985-14003, 2012.
9. S. Mariani, R. Martini, A. Ghisi, A. Corigliano, M. Beghi. Overall elastic properties of polysilicon films: a statistical investigation of the effects of polycrystal morphology. *International Journal for Multiscale Computational Engineering,* **9**, pp. 327-346, 2011.
10. S. Mariani, R. Martini, A. Corigliano, M. Beghi. Overall elastic domain of thin polysilicon films**.** *Computational Materials Science*, **50**, pp. 2993-3004, 2011.
11. A. Corigliano, M. Dossi, S. Mariani. Domain decomposition and model order reduction methods applied to the simulation of multiphysics problems in MEMS. *Computers and Structures*, **122**, pp. 113–127, 2013.
12. S. Eftekhar Azam, S. Mariani. Investigation of computational and accuracy issues in POD-based reduced order modeling of dynamic structural systems. *Engineering Structures*, **54**, pp. 150-167, 2013.
13. A. Corigliano, M. Dossi, S. Mariani. Recent advances in computational methods for microsystems. *Advanced Materials Research*, **745**, pp. 13-25, 2013.
14. A. Corigliano, R. Ardito, C. Comi, A. Frangi, A. Ghisi, S. Mariani. Microsystems and mechanics. *Procedia IUTAM*, **10**, pp. 138-160, 2014.
15. M. Bagherinia, M. Bruggi, A. Corigliano, S. Mariani, E. Lasalandra. Geometry optimization of a Lorentz force, resonating MEMS magnetometer. *Microelectronics Reliability*, **54**, pp. 1192–1199, 2014.
16. M. Bagherinia, M. Bruggi, A. Corigliano, S. Mariani, D.A. Horsley, M. Li, E. Lasalandra. An efficient earth magnetic field MEMS sensor: modeling, experimental results and optimization. *IEEE Journal of Microelectromechanical Systems*, in press.
17. A. Ghisi, S. Mariani, A. Corigliano, G. Allegato, L. Oggioni. A top-down, three-scale numerical analysis of wafer-to-wafer metallic bonding. *Microelectronics Reliability*, **54**, pp. 2039–2043, 2014.

Overview of a studied device (uni-axial MEMS accelerometer)

- Package (macro-scale)

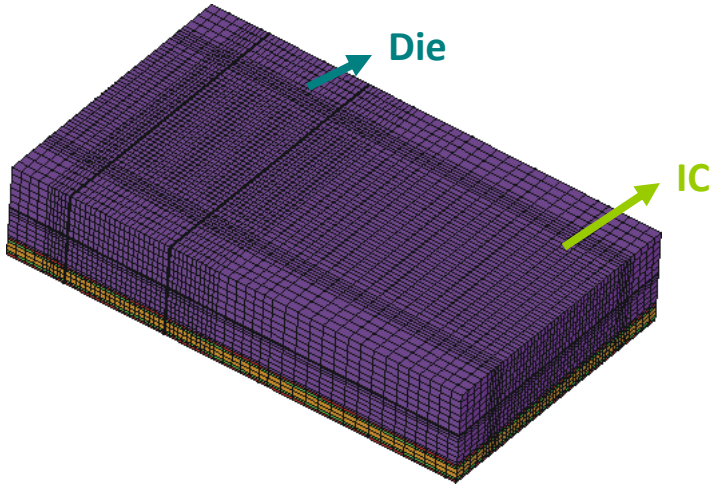

- Die (macro-scale)

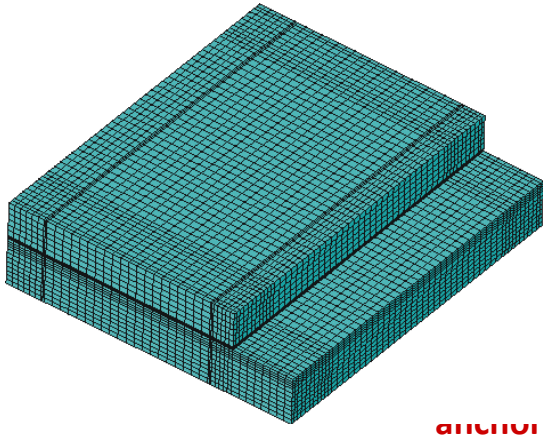

- Sensor (meso-scale)

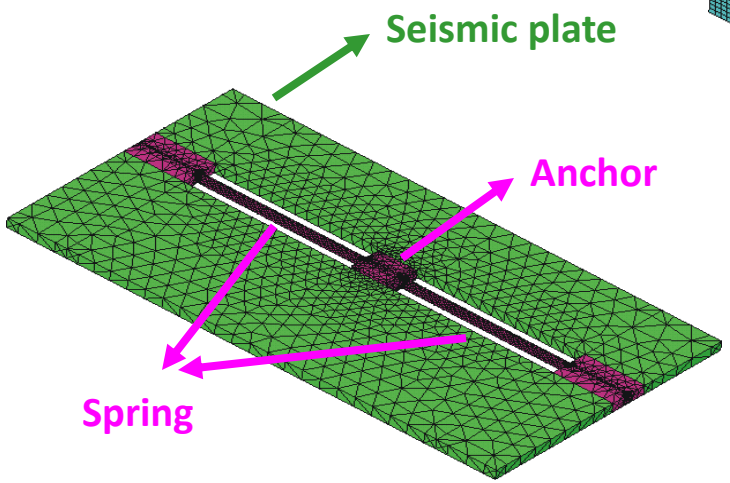

Two-scale vs three-scale analysis of drop-induced effects

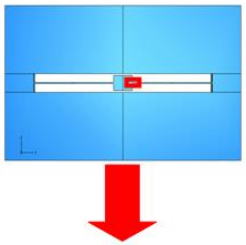

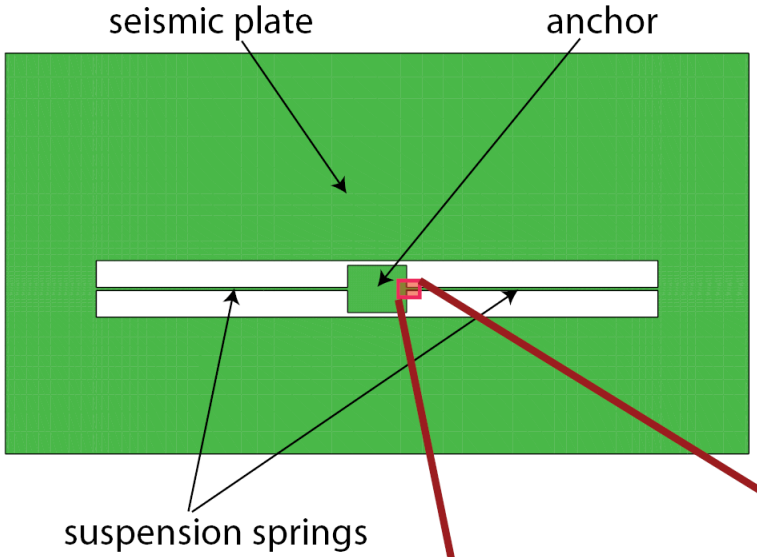

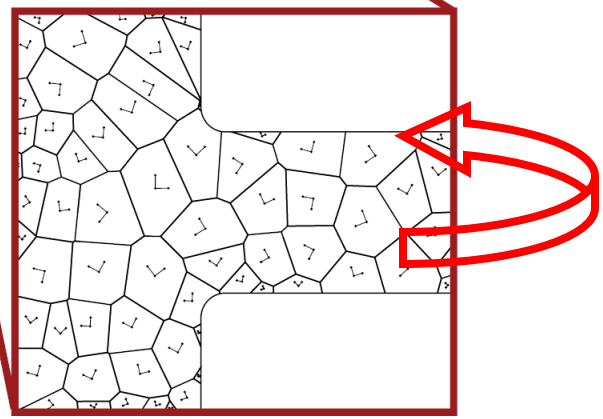

The falling direction leads to bending-dominated deformation of the suspension springs (two-dimensional analysis at micro-scale allowed)

Two-scale vs three-scale results

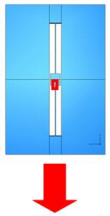

tension-dominated loading

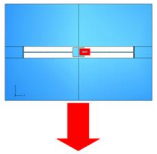

bending-dominated loading

Micro-scale:
loci of max probability of failure due to quasi-brittle cracking

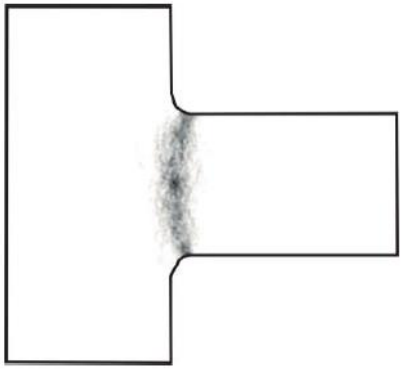

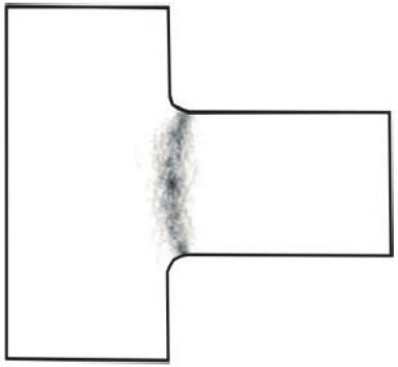

Meso-scale:
failure mode due to brittle cracking

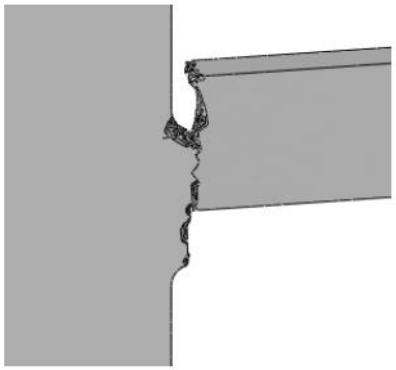

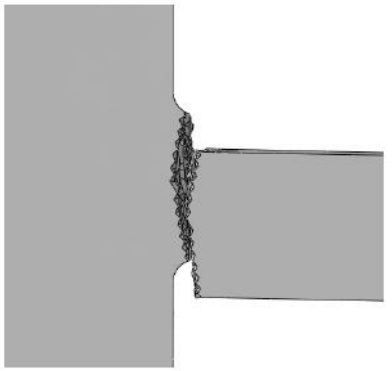

Topics to discuss:

1. Meso-scale elastic and strength properties
2. Micro-scale quasi-brittle cracking
3. Reduced-order, multi-physics modeling and optimization

Meso-scale elastic and strength properties

Micro-scale analysis: upscaling of elastic properties

Columnar polysilicon film
(lateral view)

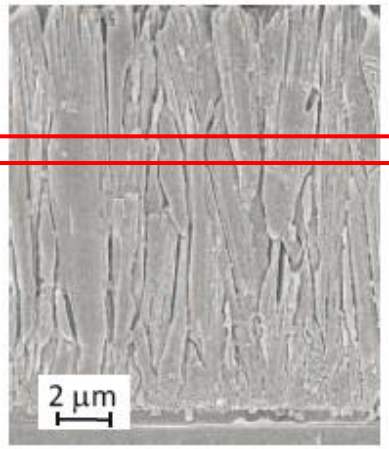

taking a slice of the film
(plane stress cond.)

regularized Voronoi tessellations

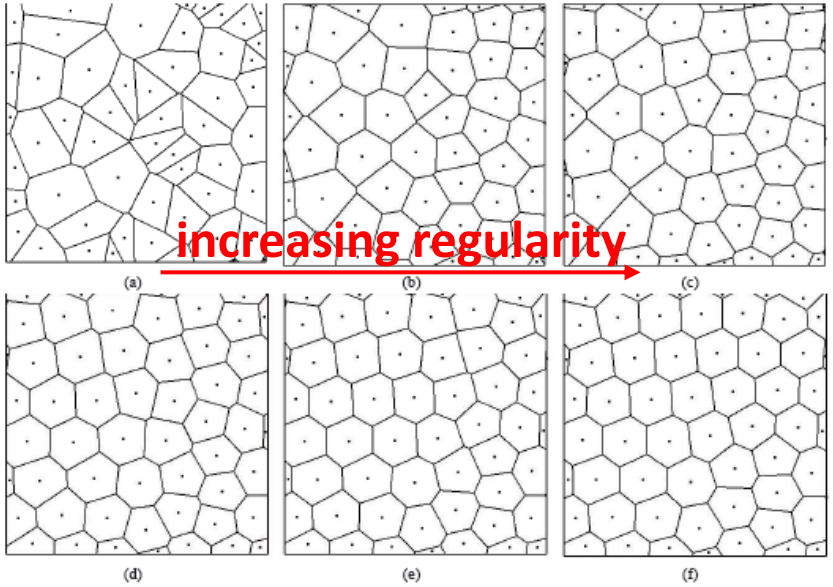

Through homogenization: in-plane macro strain and stress components (vectors)

$$\boldsymbol{E} = \{E_{11} \;\; E_{22} \;\; E_{12}\}^{\mathrm{T}}$$
$$\boldsymbol{\Sigma} = \{\Sigma_{11} \;\; \Sigma_{22} \;\; \Sigma_{12}\}^{\mathrm{T}}$$

defined as volume averages, according to:

$$\boldsymbol{\Sigma} = \frac{1}{V}\int_V \boldsymbol{\sigma} dV$$

$$\boldsymbol{E} = \frac{1}{V}\int_V \boldsymbol{\varepsilon} dV$$

local elastic law

$$\boldsymbol{\sigma} = \boldsymbol{c}\boldsymbol{\varepsilon}$$

Micro-scale: polysilicon properties

Polysilicon assumed to feature:

- one axis of elastic symmetry aligned with epitaxial growth direction x_3
- random orientation of other two elastic symmetry directions in the x_1- x_2 plane

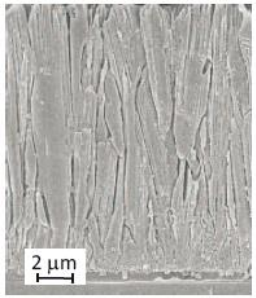

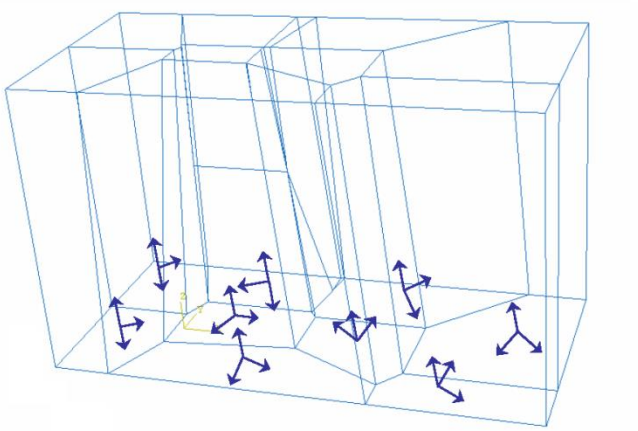

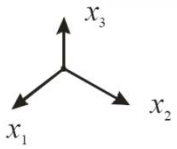

Matrix of elastic moduli for single-crystal Si (FCC symmetry)

$$\mathbf{c} = \begin{bmatrix} 165.7 & 63.9 & 63.9 & 0 & 0 & 0 \\ 63.9 & 165.7 & 63.9 & 0 & 0 & 0 \\ 63.9 & 63.9 & 165.7 & 0 & 0 & 0 \\ 0 & 0 & 0 & 79.6 & 0 & 0 \\ 0 & 0 & 0 & 0 & 79.6 & 0 \\ 0 & 0 & 0 & 0 & 0 & 79.6 \end{bmatrix} \; GPa$$

Reference value of nominal tensile strength

$$\sigma_0 = 2 \div 4 \text{ GPa}$$

Micro-scale analysis: upscaling of elastic properties

Elastic moduli in $\Sigma = CE$ are numerically bounded through:

- uniform strain boundary cond.

$$\boldsymbol{u} = \boldsymbol{X}\boldsymbol{E} \quad \text{on} \quad \partial V$$

- uniform stress boundary cond.

$$\boldsymbol{T} = \boldsymbol{N}\boldsymbol{\Sigma} \quad \text{on} \quad \partial V$$

$$\boldsymbol{X} = \begin{bmatrix} x_1 & 0 & \frac{x_2}{2} \\ 0 & x_2 & \frac{x_1}{2} \end{bmatrix}$$

$$\boldsymbol{N} = \begin{bmatrix} n_1 & 0 & n_2 \\ 0 & n_2 & n_1 \end{bmatrix}$$

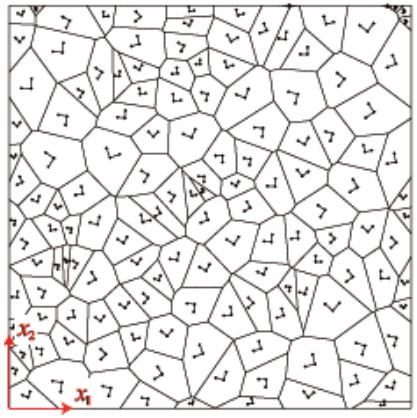

Voigt and **Reuss** bounds:
from Hill-Mandel macro-homogeneity condition $\boldsymbol{\Sigma}^{\mathrm{T}}\boldsymbol{E} = \frac{1}{V}\int_V \boldsymbol{\sigma}^{\mathrm{T}}\boldsymbol{\varepsilon}\,dV = \frac{1}{V}\int_V \boldsymbol{\sigma}_l^{\mathrm{T}}\boldsymbol{\varepsilon}_l\,dV$

Voigt assumption: $\boldsymbol{\varepsilon} = \boldsymbol{E}$ everywhere

$$\boldsymbol{E}^{\mathrm{T}}\boldsymbol{C}\boldsymbol{E} = \frac{1}{V}\int_V \boldsymbol{\varepsilon}_l^{\mathrm{T}}\boldsymbol{c}_l\boldsymbol{\varepsilon}_l\,dV = \frac{1}{V}\int_V \boldsymbol{\varepsilon}^{\mathrm{T}}\boldsymbol{t}_\varepsilon^{\mathrm{T}}\boldsymbol{c}_l\boldsymbol{t}_\varepsilon\boldsymbol{\varepsilon}\,dV = \boldsymbol{E}^{\mathrm{T}}\left[\frac{1}{V}\int_V \boldsymbol{t}_\varepsilon^{\mathrm{T}}\boldsymbol{c}_l\boldsymbol{t}_\varepsilon\,dV\right]\boldsymbol{E} = \boldsymbol{E}^{\mathrm{T}}\left[\frac{1}{V}\int_V \boldsymbol{c}\,dV\right]\boldsymbol{E}$$

$$\Rightarrow \quad \boldsymbol{C} = \frac{1}{V}\int_V \boldsymbol{t}_\varepsilon^{\mathrm{T}}\boldsymbol{c}_l\boldsymbol{t}_\varepsilon\,dV$$

Reuss assumption: $\boldsymbol{\sigma} = \boldsymbol{\Sigma}$ everywhere $\quad \Rightarrow \quad \boldsymbol{C}^{-1} = \frac{1}{V}\int_V \boldsymbol{t}_\sigma^{\mathrm{T}}\boldsymbol{c}_l^{-1}\boldsymbol{t}_\sigma\,dV$

Micro-scale analysis: upscaling of elastic properties

$L = 12\ \mu\text{m},$
$\bar{s}_g = 0.2\ \mu\text{m}$

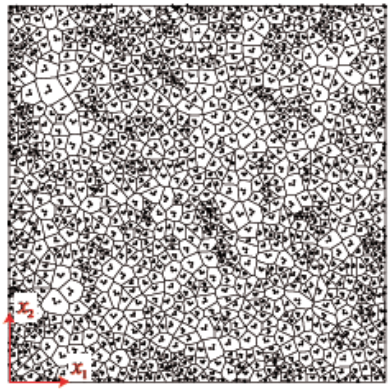

$\boldsymbol{u} = \boldsymbol{X}\boldsymbol{E}$ on ∂V

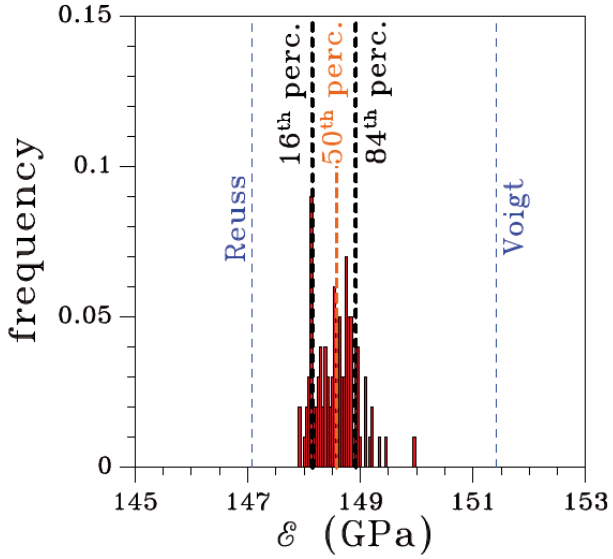

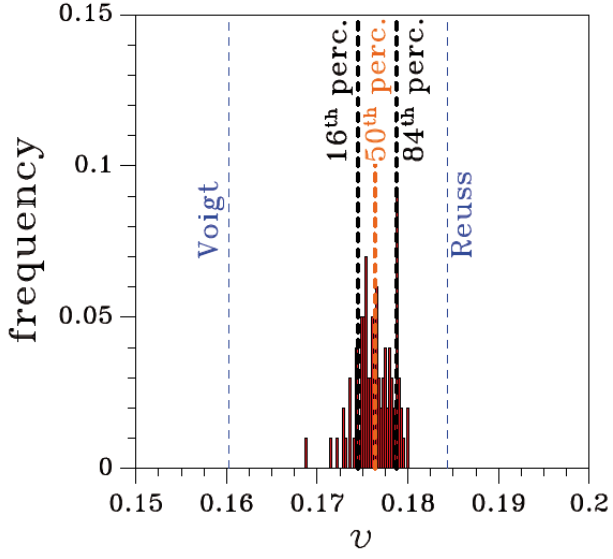

$\boldsymbol{T} = \boldsymbol{N}\boldsymbol{\Sigma}$ on ∂V

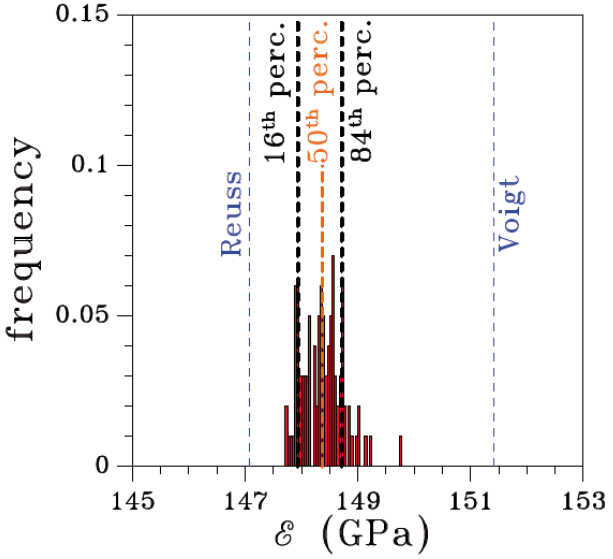

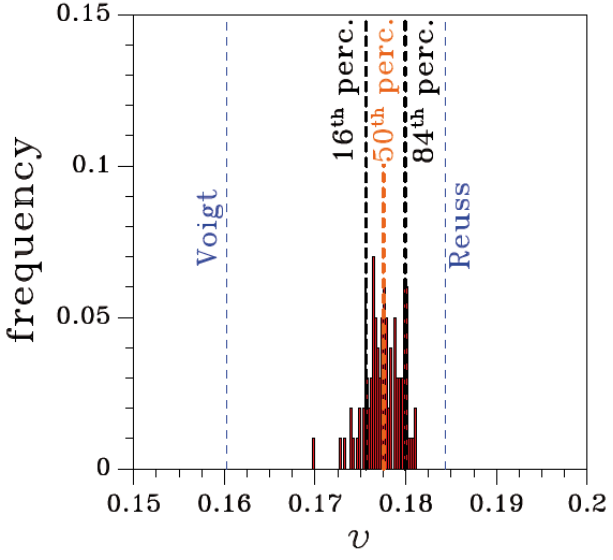

Micro-scale analysis: upscaling of elastic properties

$L = 12\ \mu\text{m},$
$\bar{s}_g = 0.6\ \mu\text{m}$

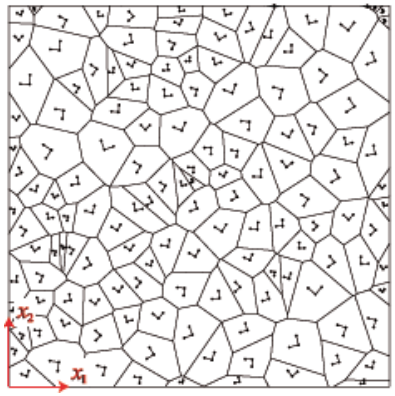

$\boldsymbol{u} = \boldsymbol{X}\boldsymbol{E}$ on ∂V

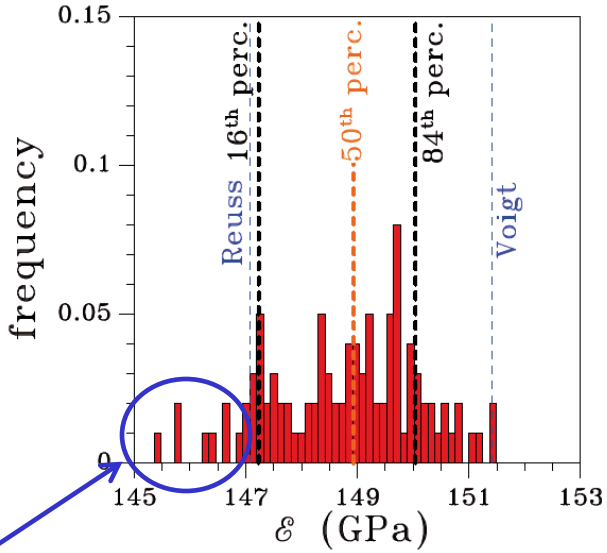

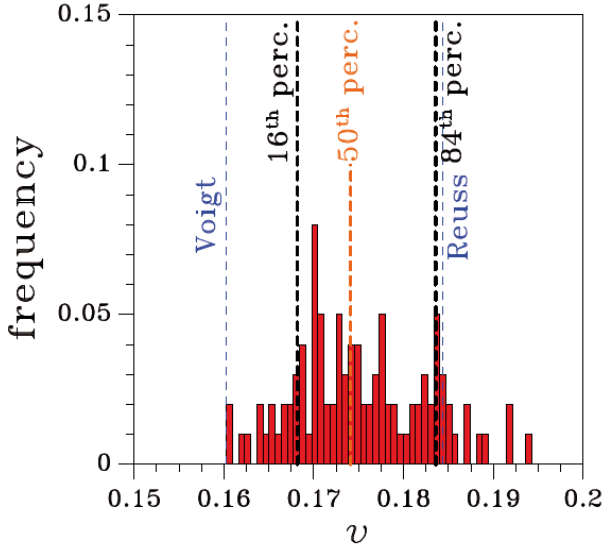

Results exceeding bounds (why?)

$$\boldsymbol{C} = \frac{1}{V}\int_V \boldsymbol{t}_\varepsilon^{\mathrm{T}} \boldsymbol{c}_l \boldsymbol{t}_\varepsilon \, dV$$

$\boldsymbol{T} = \boldsymbol{N}\boldsymbol{\Sigma}$ on ∂V

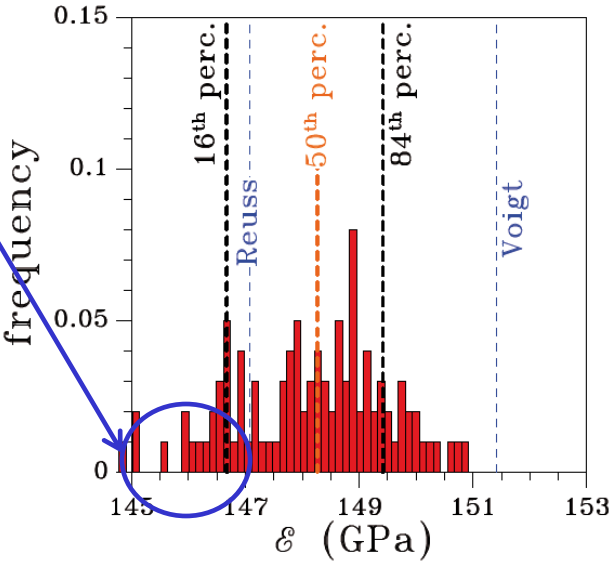

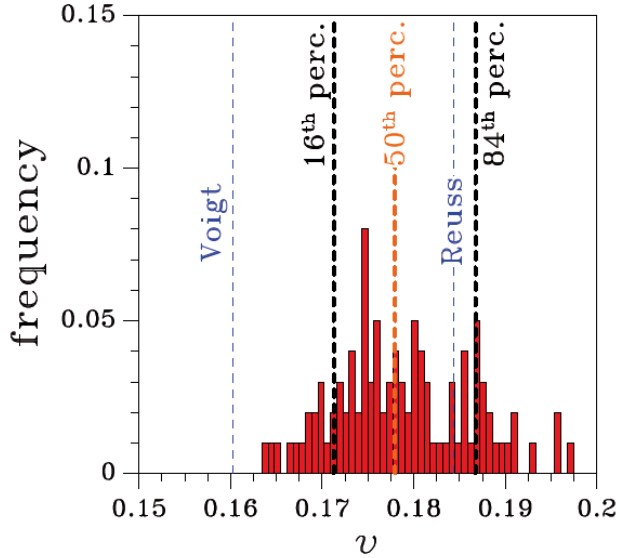

RVE size and upscaling of elastic properties

$$\boldsymbol{u} = \boldsymbol{X}\boldsymbol{E} \quad \text{on} \quad \partial V$$

$\bar{s}_g = 0.6$ μm

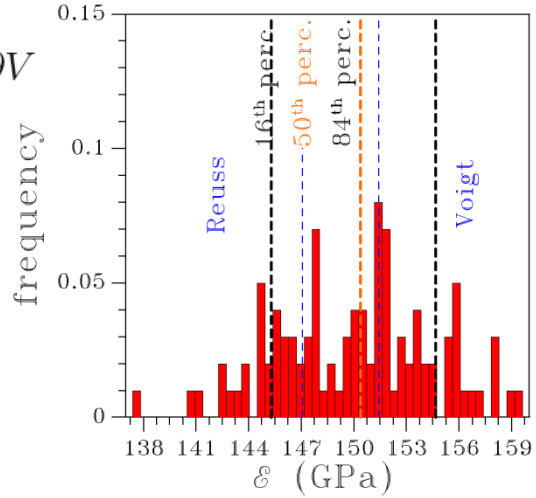

$L = 3$ μm

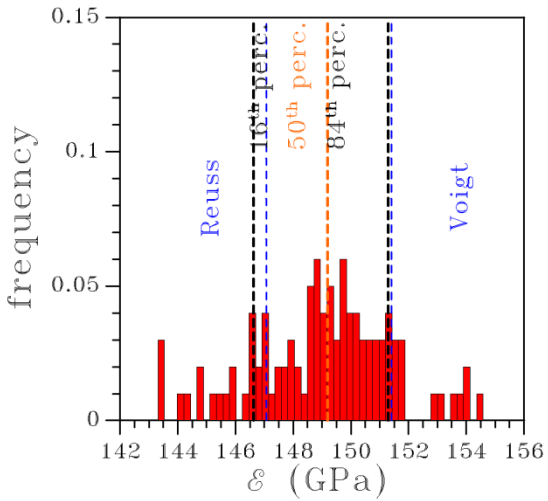

$L = 6$ μm

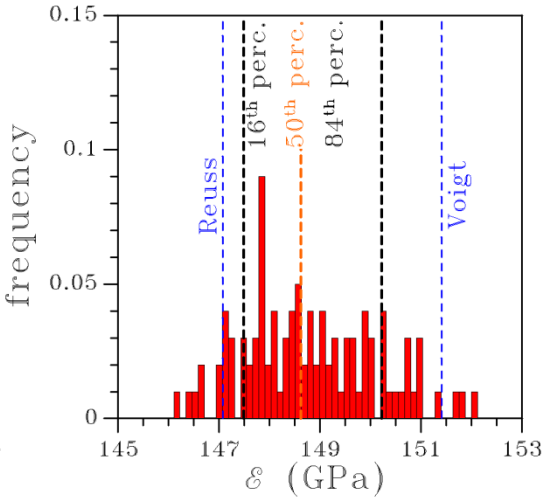

$L = 12$ μm

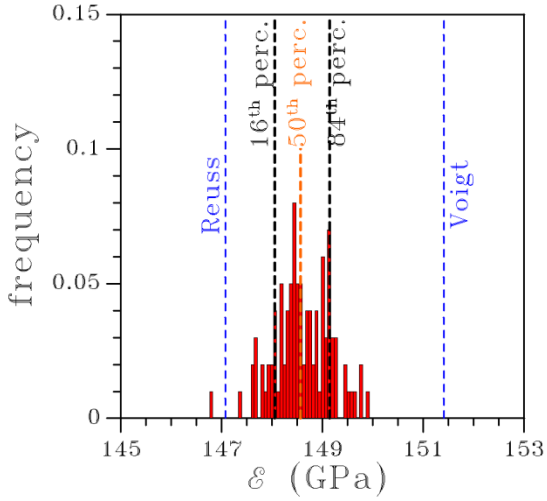

$L = 24$ μm

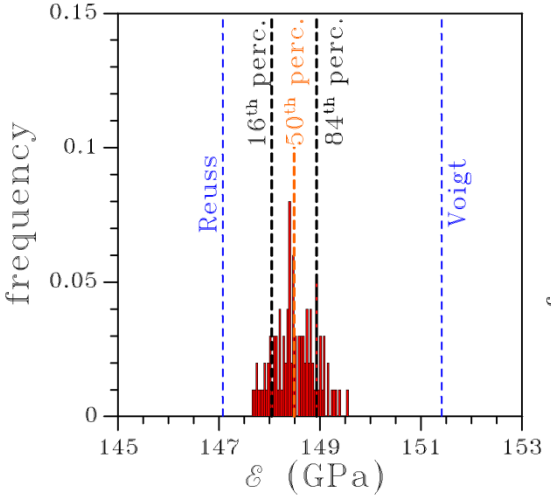

$L = 36$ μm

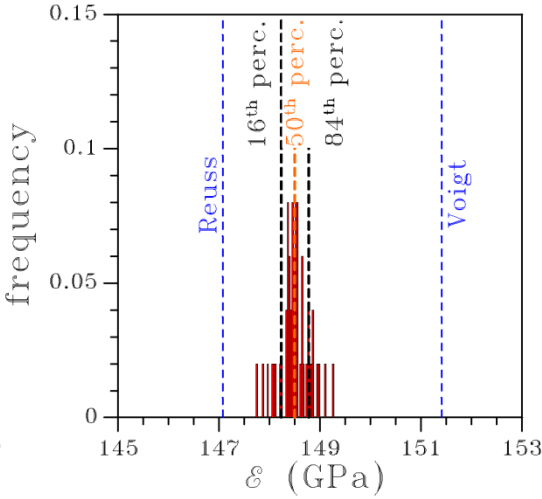

$L = 48$ μm

RVE size and upscaling of elastic properties

$\boldsymbol{T} = \boldsymbol{N}\boldsymbol{\Sigma}$ on ∂V

$\bar{s}_g = 0.6$ μm

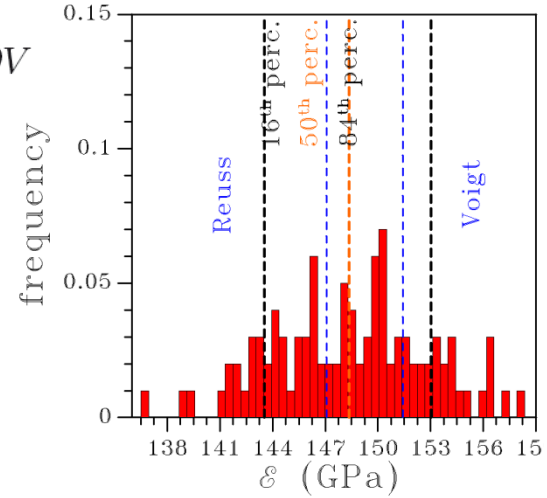

$L = 3$ μm

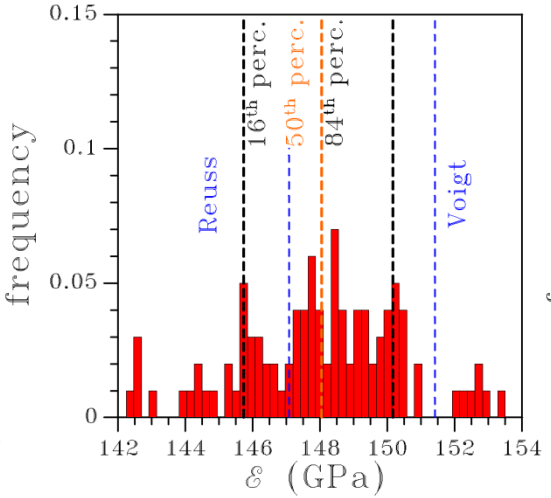

$L = 6$ μm

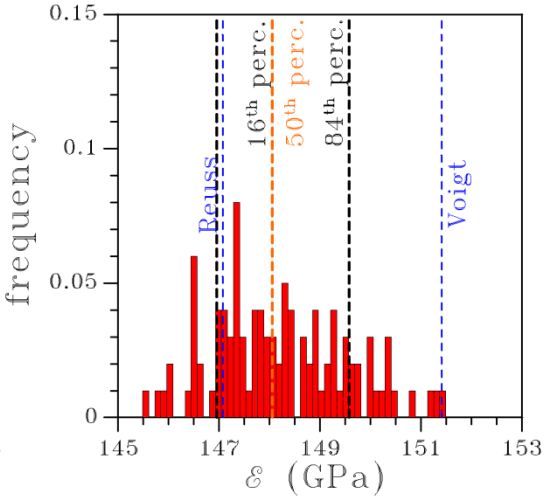

$L = 12$ μm

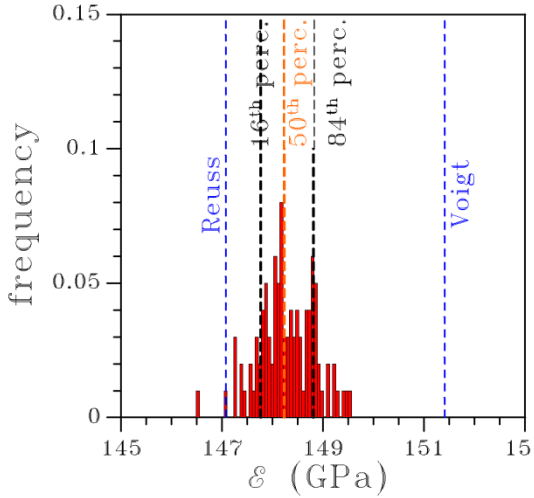

$L = 24$ μm

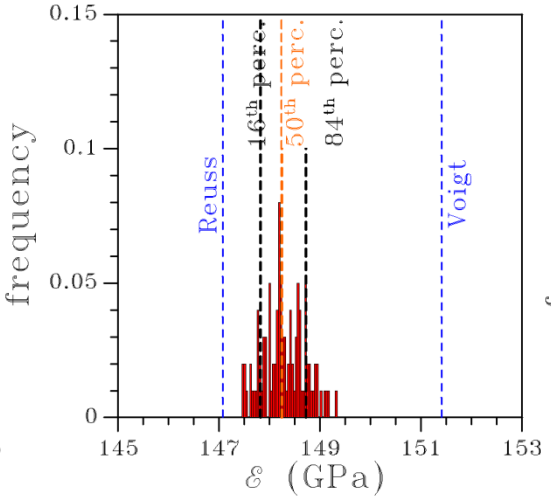

$L = 36$ μm

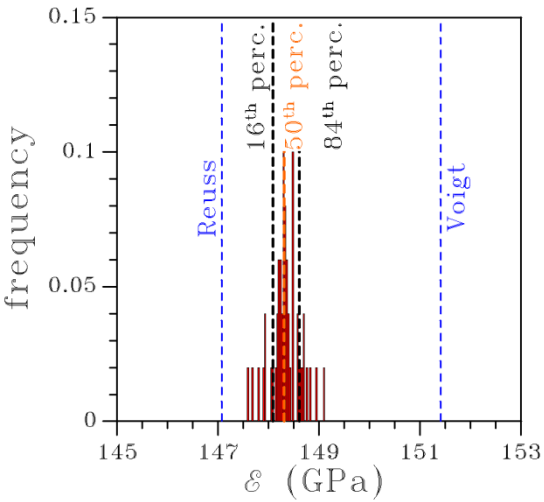

$L = 48$ μm

Micro-scale analysis: upscaling of elastic properties

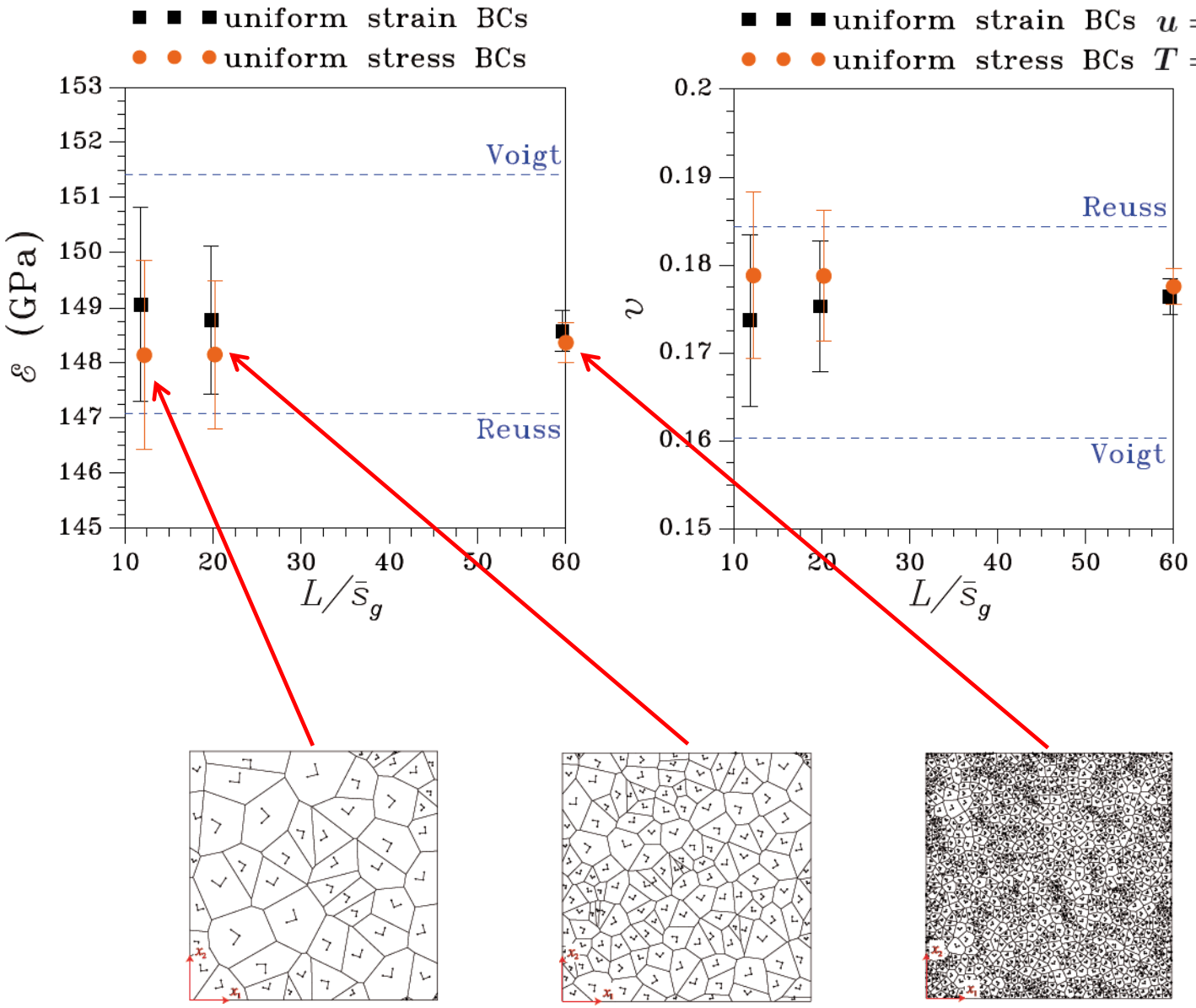

Lattice orientation statistics for different RVE sizes

$$\boldsymbol{C} = \frac{1}{V}\int_V \boldsymbol{t}_\varepsilon^{\mathrm{T}} \boldsymbol{c}_l \boldsymbol{t}_\varepsilon \, dV$$

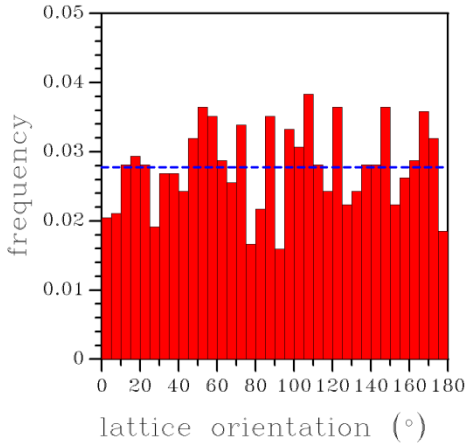

$L = 3$ µm

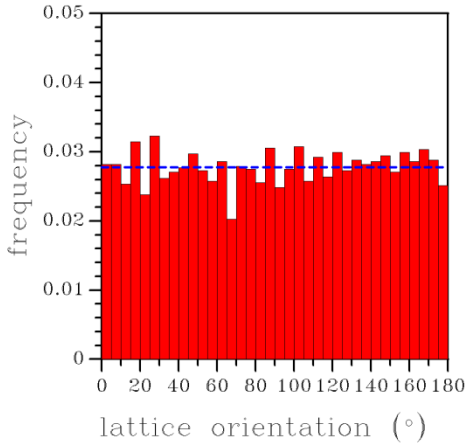

$L = 6$ µm

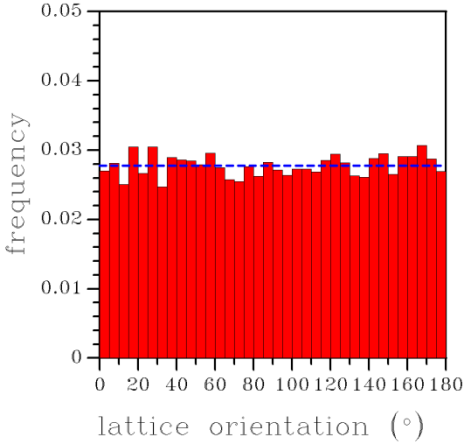

$L = 12$ µm

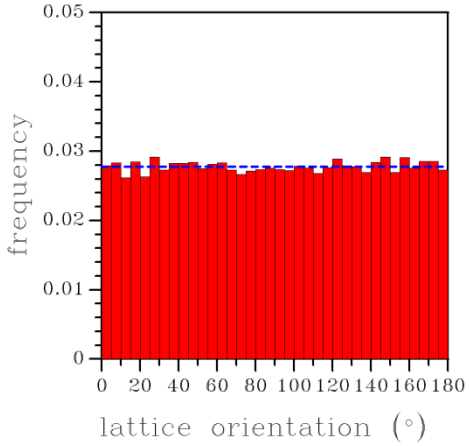

$L = 24$ µm

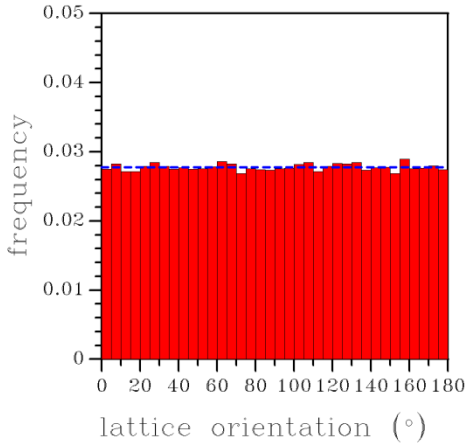

$L = 36$ µm

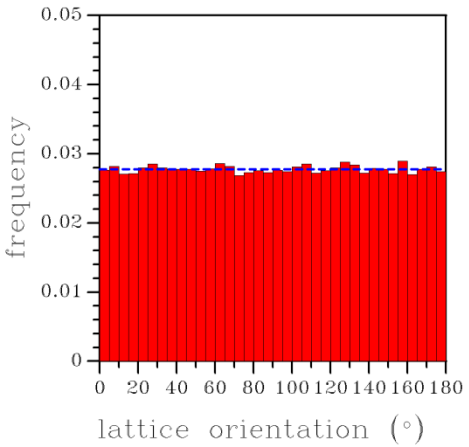

$L = 48$ µm

Regularization and upscaling of elastic properties

$u = XE$ on ∂V

$L = 12$ μm

$L = 24$ μm

$L = 48$ μm

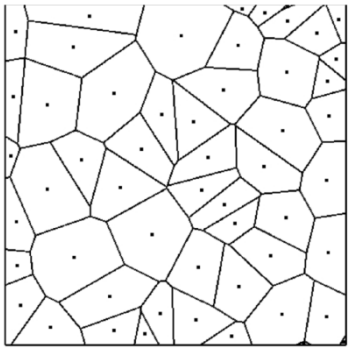

No Regularization

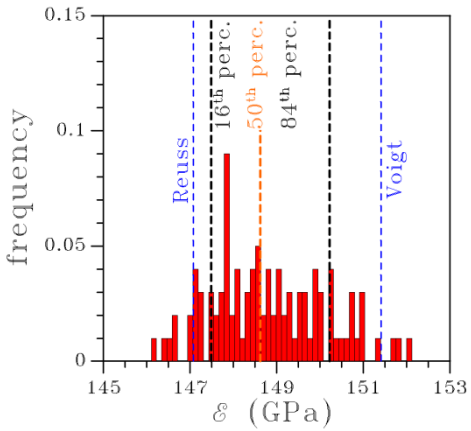

$Median = 148.62$ GPa

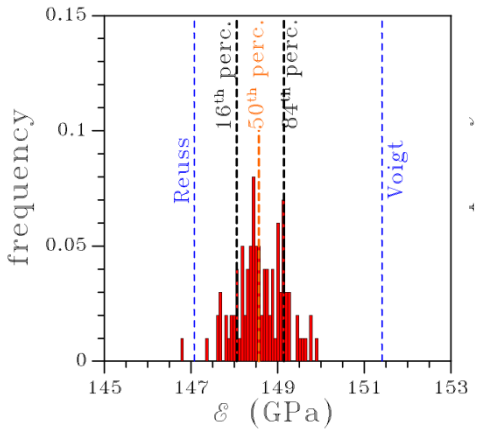

$Median = 148.56$ GPa

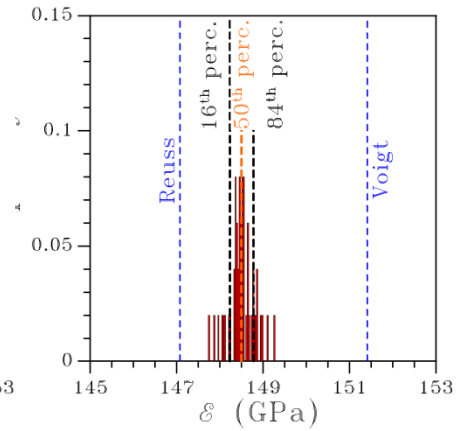

$Median = 148.50$ GPa

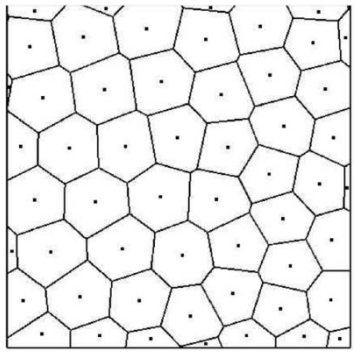

20 *Regularization*

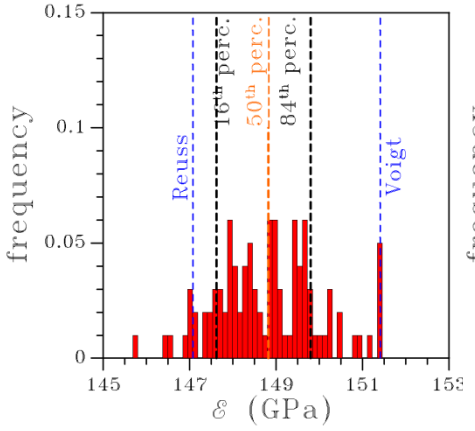

$Median = 148.82$ GPa

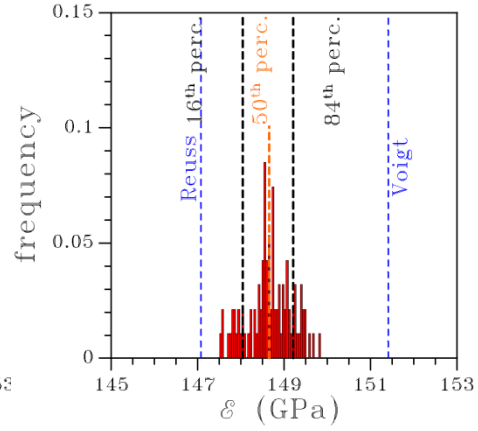

$Median = 148.65$ GPa

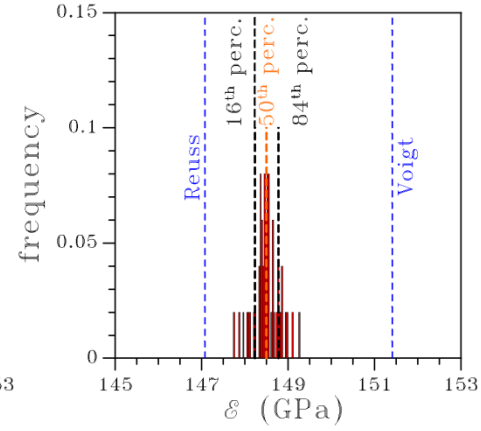

$Median = 148.50$ GPa

Micro-scale analysis: upscaling of elastic domain (strength)

Elastic domain of single-crystal Si (plane-stress)

3D view

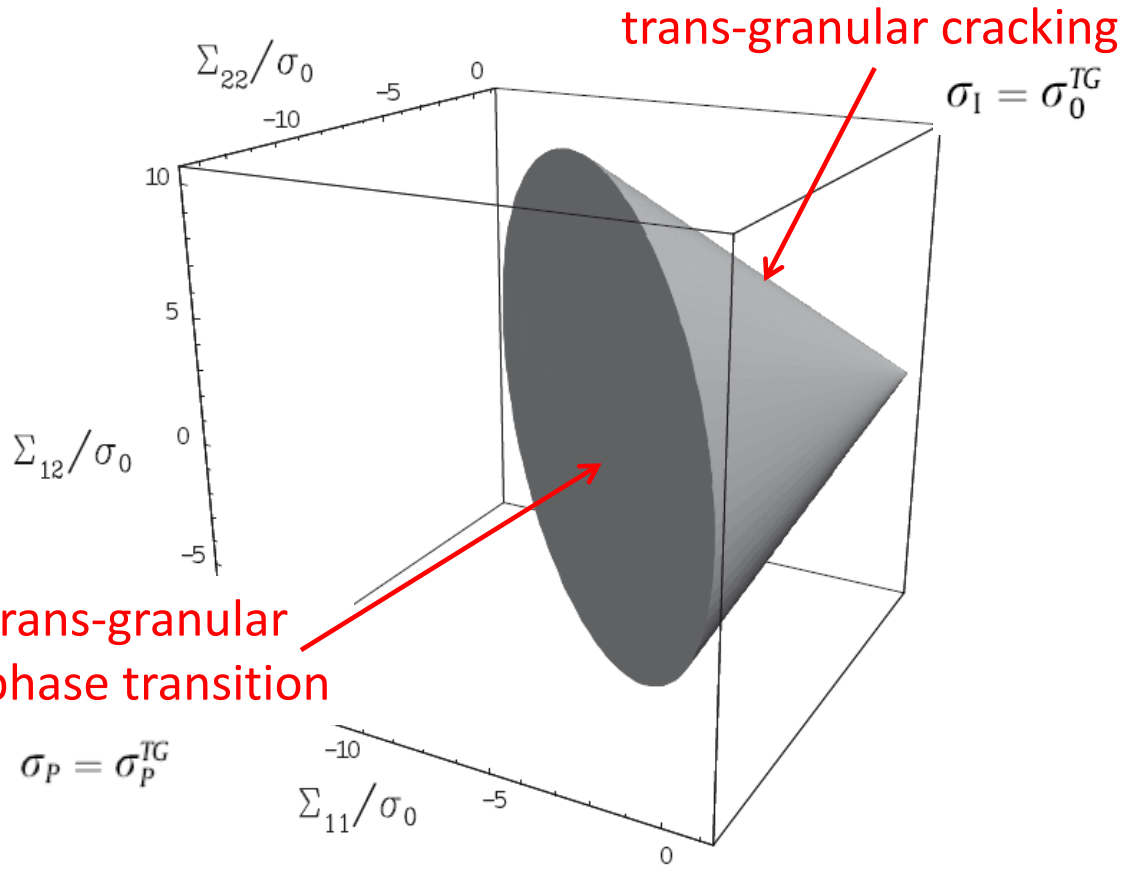

projections

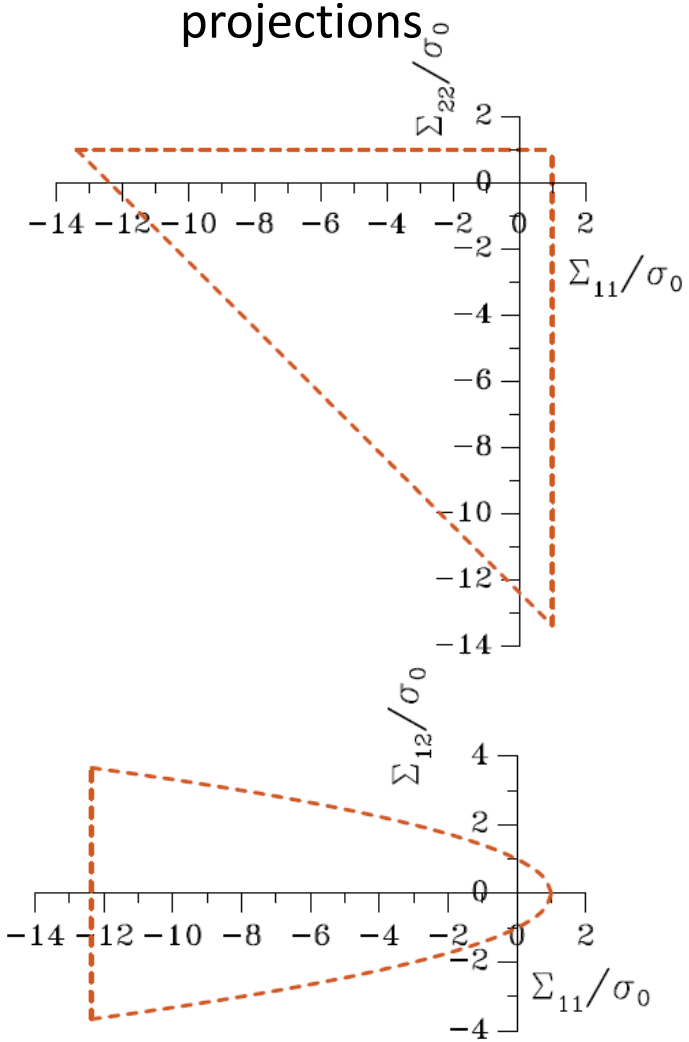

Micro-scale analysis: upscaling of elastic domain (strength)

Adding the inter-granular cracking condition [Camacho-Ortiz], under uniform strain BCs

$$\sigma = \sqrt{\langle \sigma_n \rangle^2 + \frac{1}{\beta^2}\sigma_s^2} = \sigma_0^{IG}$$

normal traction component

shear traction component

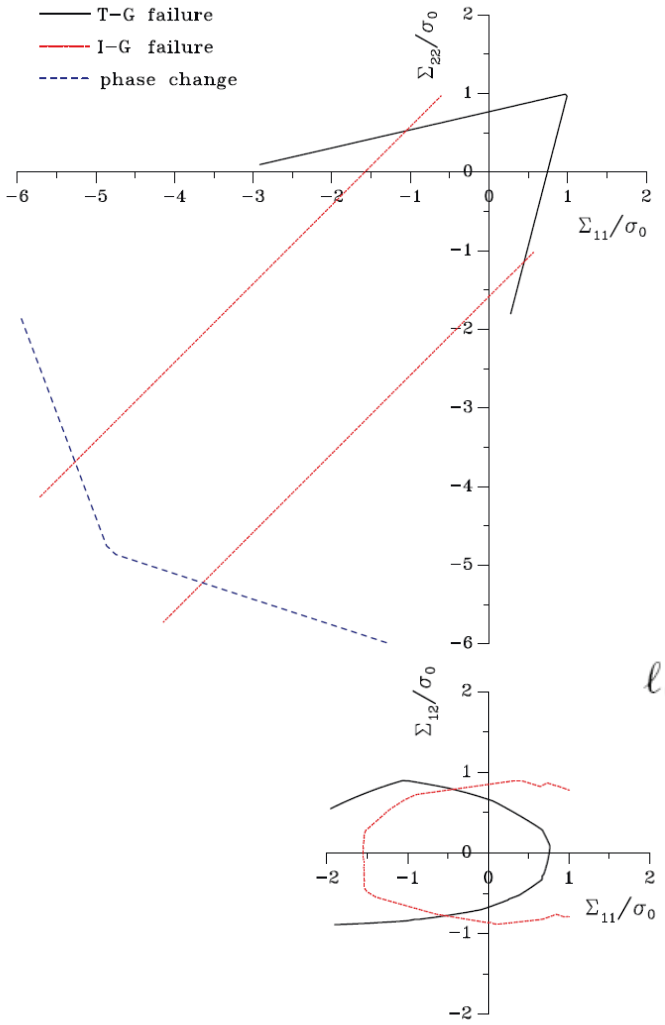

$$\ell_{\text{cohe}} = \frac{1}{\pi}\frac{EG_c^t}{\tau_M^{t2}} \approx 22\,\text{nm}$$

adopted space discretization to resolve stress-state along GBs

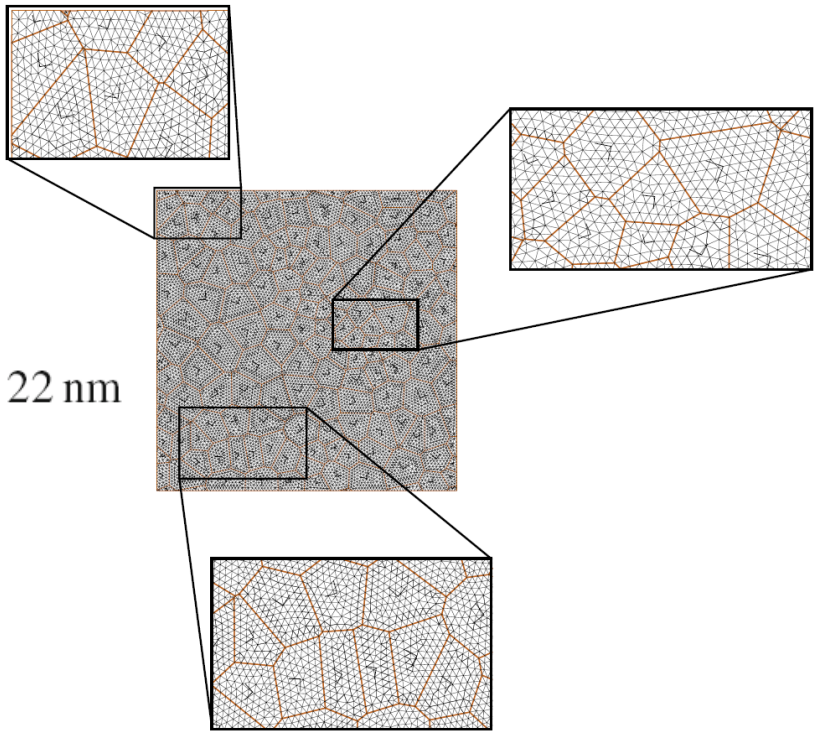

Micro-scale analysis: upscaling of elastic domain (strength)

Effect of RVE size on the shape of elastic domain ($d_e = 0.2\ \mu\text{m}$)

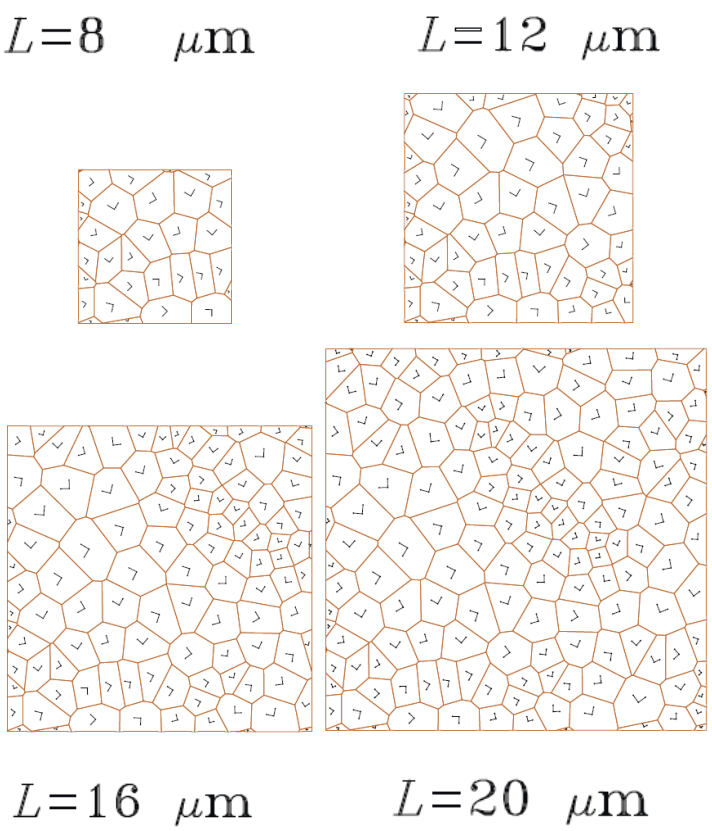

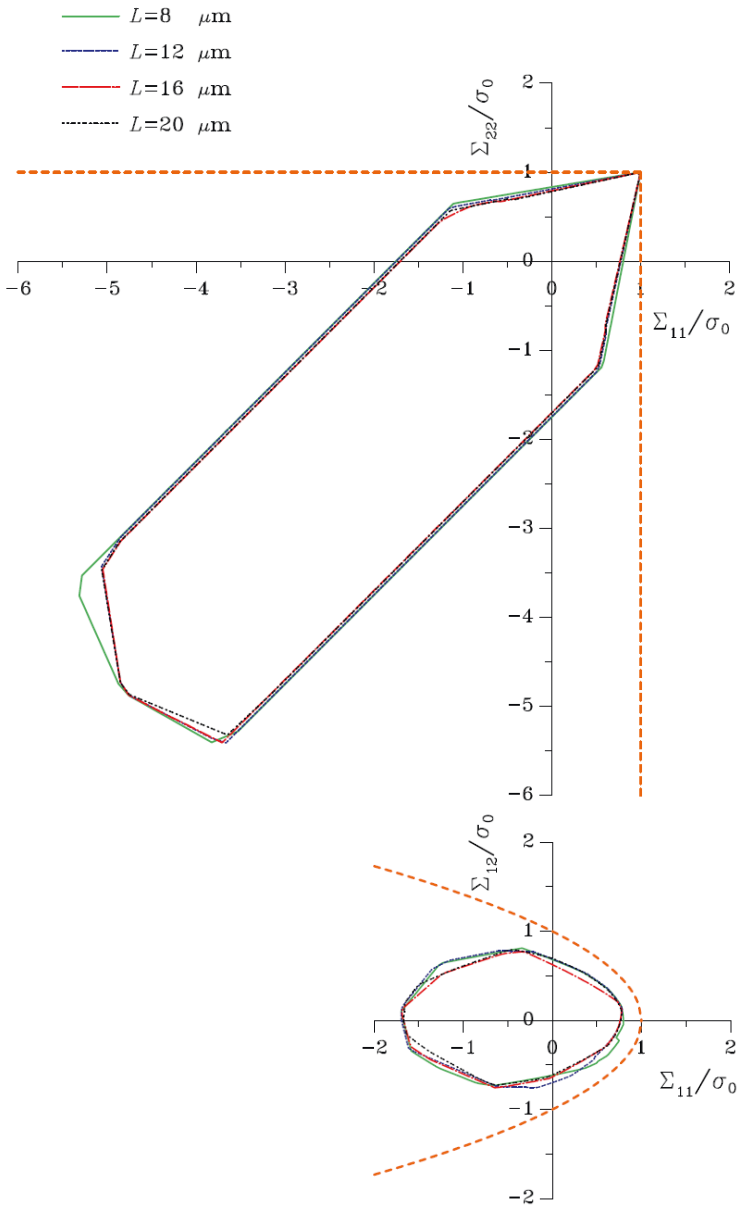

Micro-scale quasi-brittle cracking

Statics of quasi-brittle materials: principle of virtual power

Weak form of incremental equilibrium

$$\int_{\Omega\setminus\Gamma_d} \boldsymbol{\gamma}^{\mathrm{T}}\dot{\boldsymbol{\sigma}}\,\mathrm{d}\Omega = \int_{\Omega\setminus\Gamma_d} \boldsymbol{v}^{\mathrm{T}}\dot{\bar{\boldsymbol{b}}}\,\mathrm{d}\Omega + \int_{\Gamma_t} \boldsymbol{v}^{\mathrm{T}}\dot{\bar{\boldsymbol{t}}}\,\mathrm{d}\Gamma_t - \int_{\Gamma_d} [\boldsymbol{v}]^{\mathrm{T}}\dot{\boldsymbol{t}}\,\mathrm{d}\Gamma_d \qquad \forall \boldsymbol{v} \in \mathcal{U}_0$$

$\boldsymbol{v}$ is the test function

$\boldsymbol{\gamma} = \boldsymbol{\mathcal{C}}\boldsymbol{v}$

$\mathcal{U}$ is the trial solution space
($\boldsymbol{u}$ continuous in $\Omega\setminus\Gamma_d$, possibly discontinuous along Γ_d)

$\mathcal{U}_0$ is the variation space
($\boldsymbol{v}$ continuous in $\Omega\setminus\Gamma_d$, possibly discontinuous along Γ_d, $\boldsymbol{v}=\boldsymbol{0}$ on Γ_u)

Allowing for bulk and interface constitutive models

$$\text{find } \boldsymbol{u} \in \mathcal{U}: \quad \int_{\Omega\setminus\Gamma_d} \boldsymbol{\gamma}^{\mathrm{T}}\boldsymbol{E}_{\Omega}(\boldsymbol{x})\,\boldsymbol{\varepsilon}\,\mathrm{d}\Omega + \int_{\Gamma_d} [\boldsymbol{v}]^{\mathrm{T}}\boldsymbol{E}_{\Gamma}(\boldsymbol{x})\,[\dot{\boldsymbol{u}}]\,\mathrm{d}\Gamma_d$$

$$= \int_{\Omega\setminus\Gamma_d} \boldsymbol{v}^{\mathrm{T}}\dot{\bar{\boldsymbol{b}}}\,\mathrm{d}\Omega + \int_{\Gamma_t} \boldsymbol{v}^{\mathrm{T}}\dot{\bar{\boldsymbol{t}}}\,\mathrm{d}\Gamma_t \quad \forall \boldsymbol{v} \in \mathcal{U}_0$$

Cohesive model (TG and IG cracking)

Effective displacement discontinuity [Camacho&Ortiz]:

$$[u] = \sqrt{[u]_n^2 + \beta^2 [u]_s^2}$$

opening (mode I) component

sliding (mode II) component

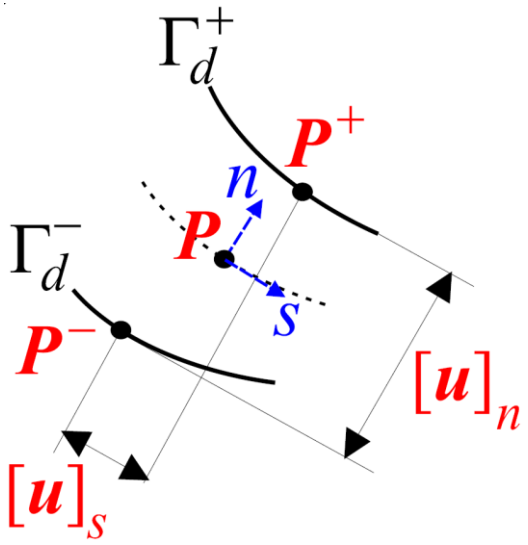

work conjugate effective traction:

$$t = \sqrt{t_n^2 + \frac{1}{\beta^2} t_s^2}$$

Irreversible effective cohesive law

- linear envelope: $t = t^{\max}\left(1 - \frac{[u]}{[u]^{\max}}\right)$
- unloading to the origin of the t-$[u]$ plane;
- fracture energy: $G = t^{\max}[u]^{\max}/2$

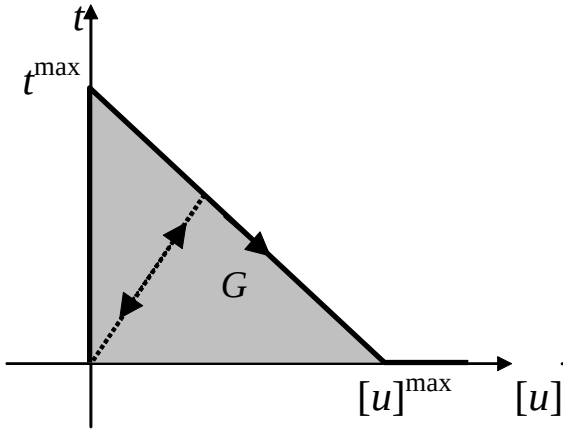

Micro-scale analysis: anisotropic TG fracture energy

[Tanaka *et alii*, IJF]

- Transgranular fracture energy *assumed* to smoothly vary, depending on the relative orientation of crack plane and grain crystal lattice
- Transgranular strength independent of the orientation

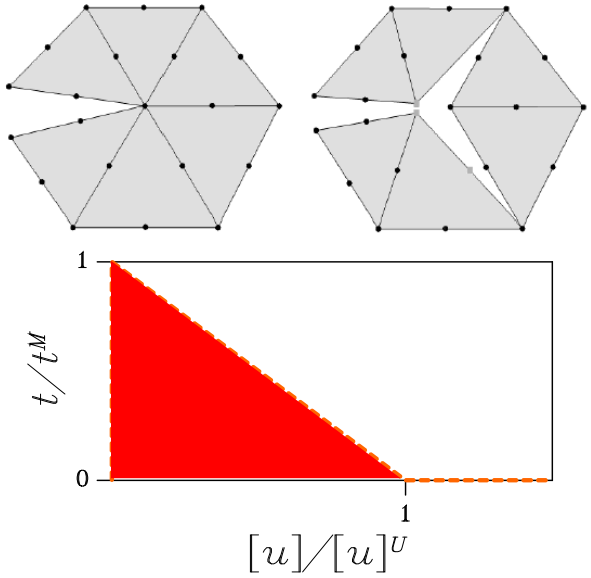

Experimental data by Tanaka et al., IJF 2006

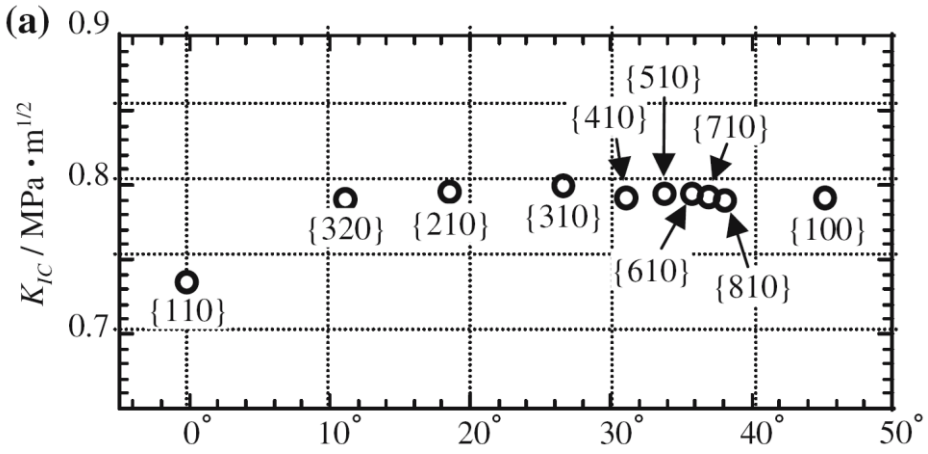

2D simulations

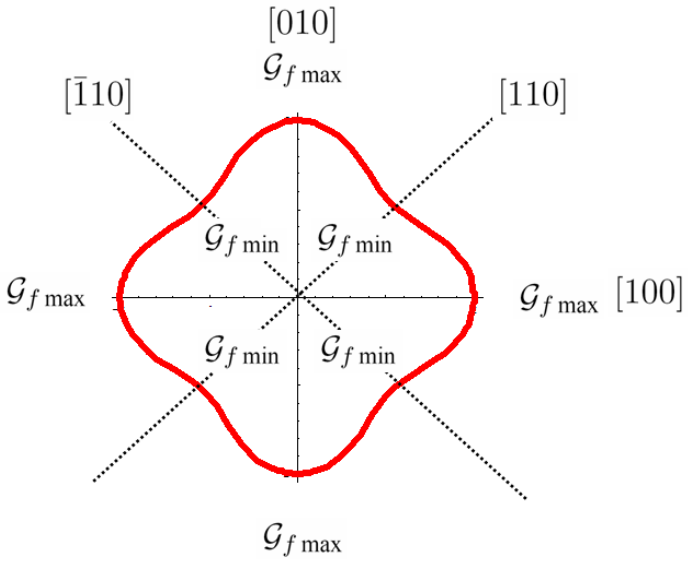

2D micro-scale analysis: typical crack evolution

Depending on the falling orientation,
crack may start from one of the two reentrant corners
at the end of each suspension spring

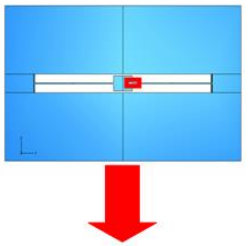

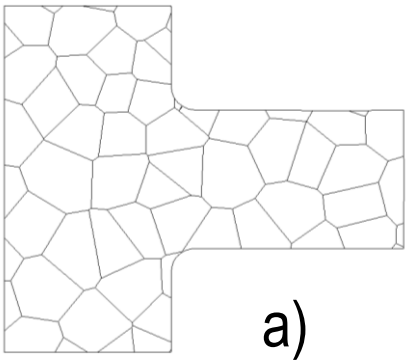

a)

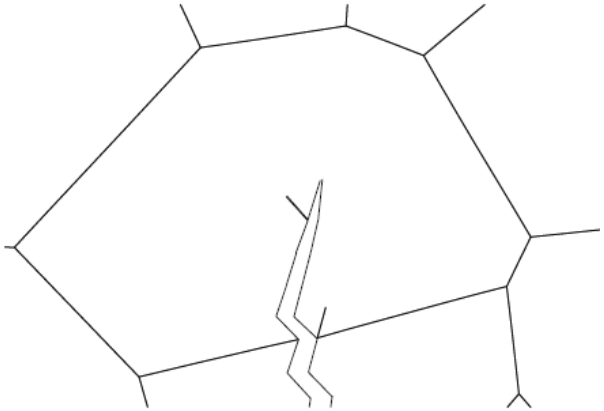

(a)

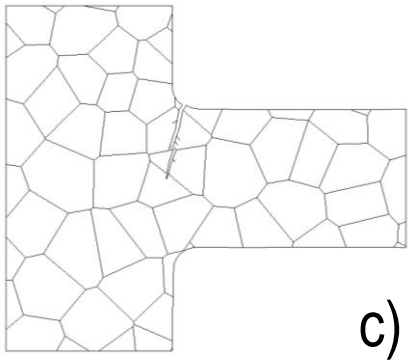

c)

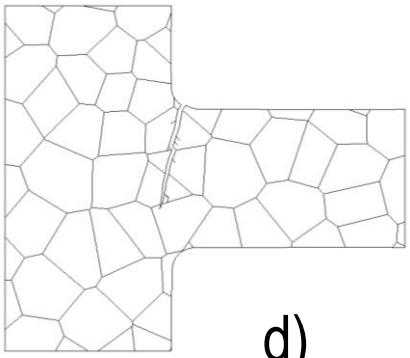

d)

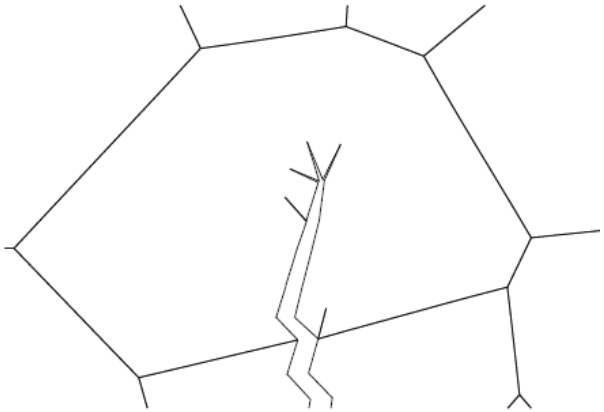

(b)

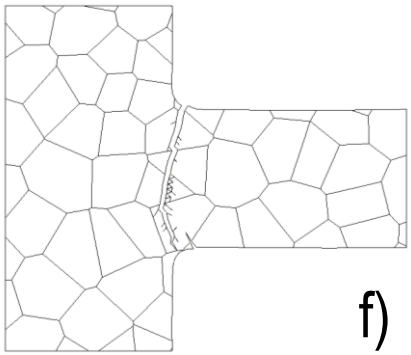

f)

Micro-scale analysis: Monte Carlo simulations

Monte Carlo simulations are carried out with different grain morphologies and crystal orientations

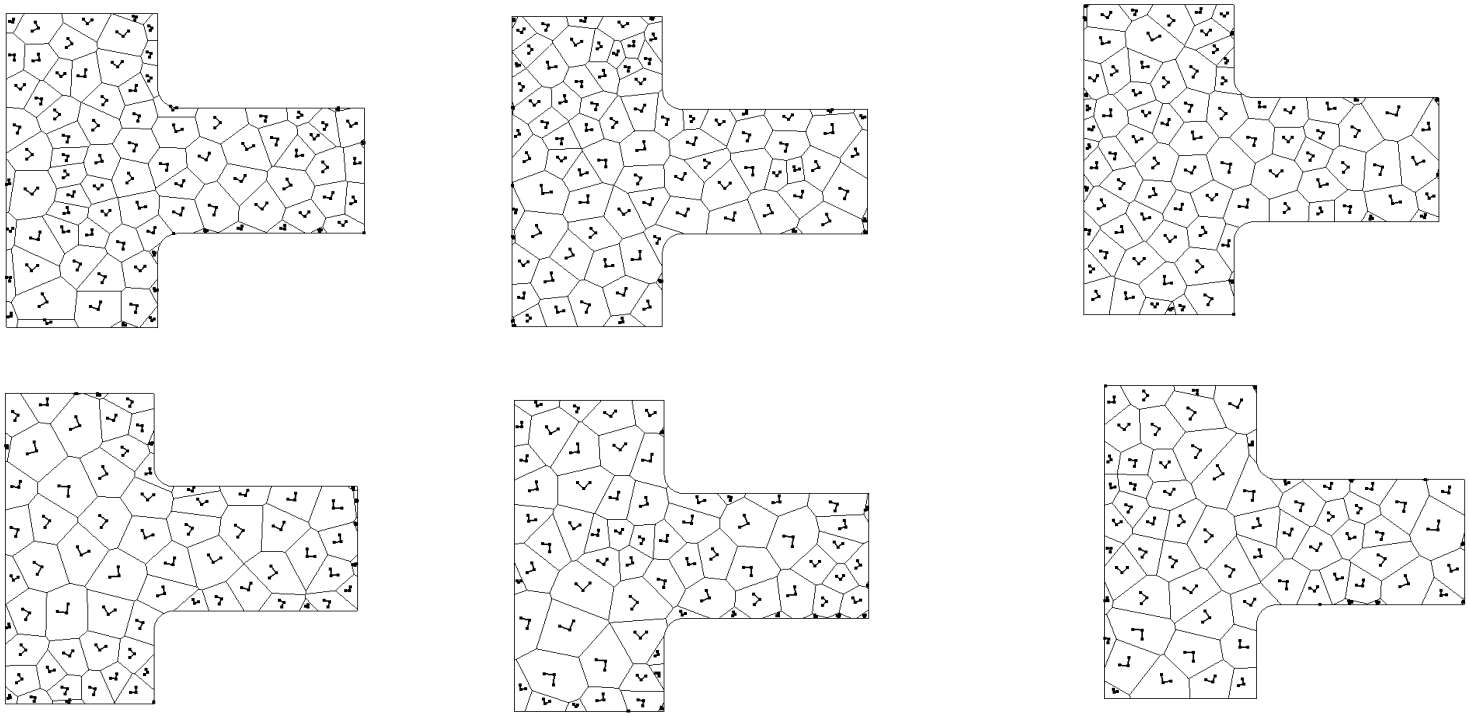

tessellation

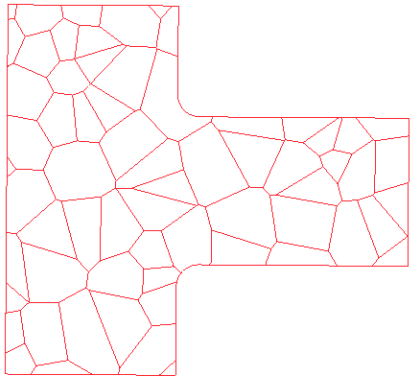

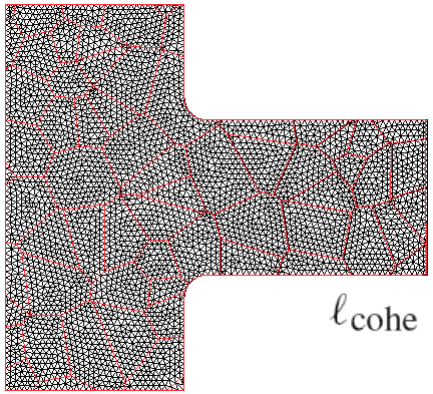

FE mesh

$$\ell_{\text{cohe}} = \frac{1}{\pi}\frac{EG_c^t}{\tau_M^{t2}} \approx 22\,\text{nm}$$

Micro-scale analysis: forecast of crack path at failure

Failure probability map:
at convergence of the statistics of the Monte Carlo simulation, map of probability for a crack to pass by that point

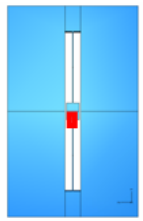

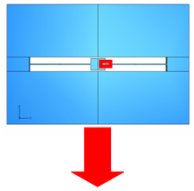

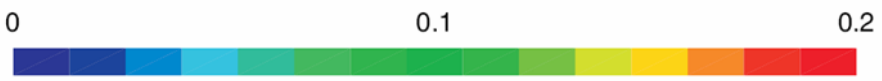

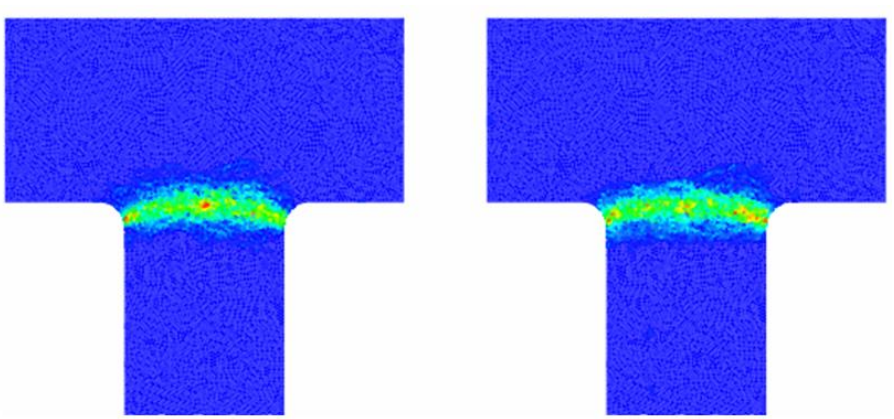

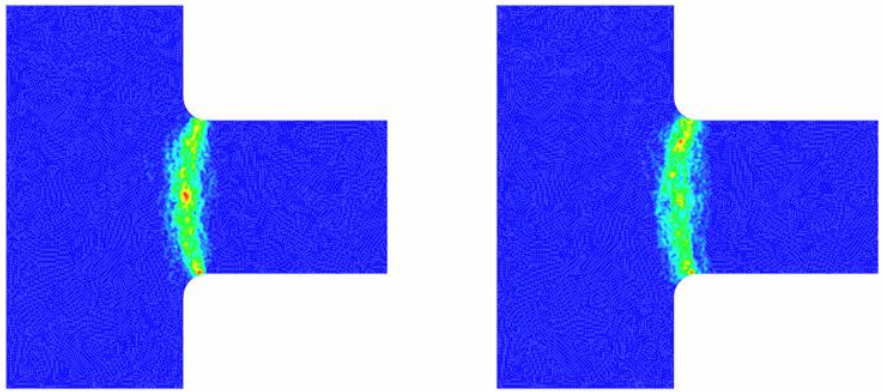

Reduced (-20%) tensile strength at grain boundaries

Reduced (-20%) tensile strength at grain boundaries

Micro-scale analysis: forecast of crack speed

Statistics of crack speed:

median value around 100-200 (m/s) due to continuous branching

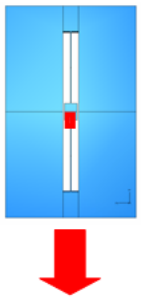

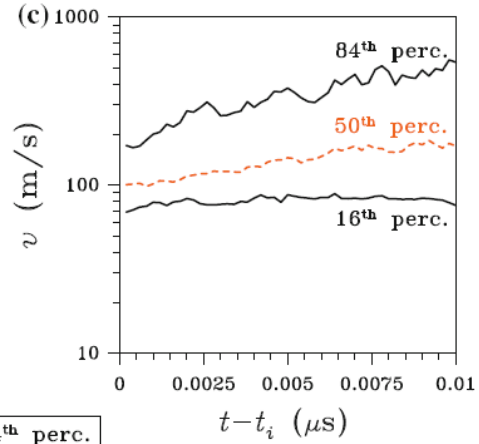

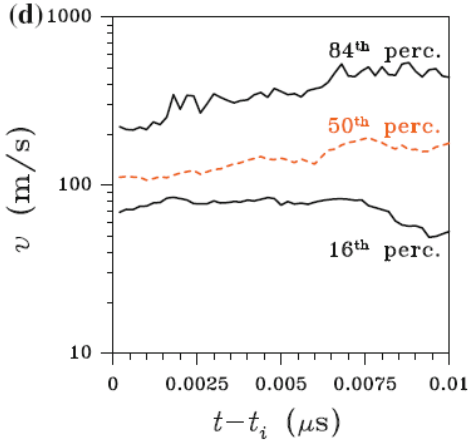

Reduced (-20%) tensile strength at grain boundaries

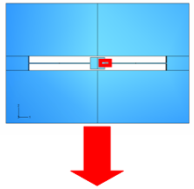

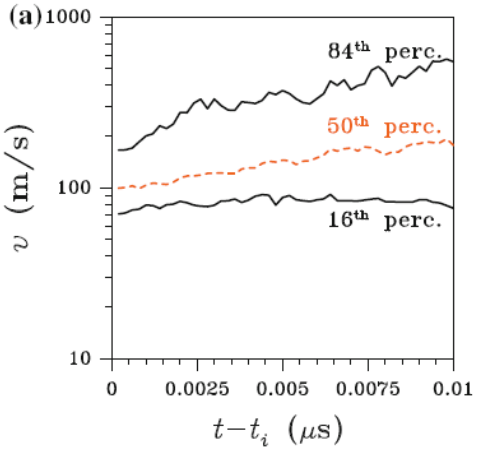

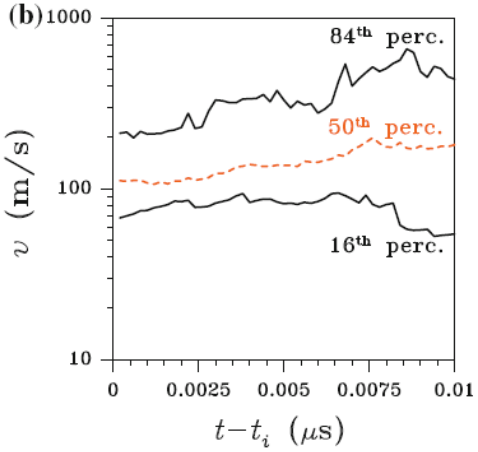

Reduced (-20%) tensile strength at grain boundaries

Micro-scale analysis: on-chip testing (crack and fatigue)

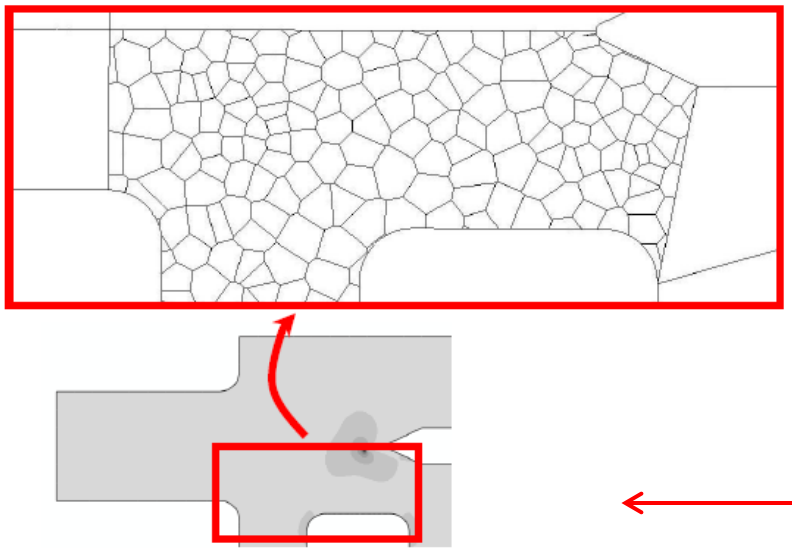

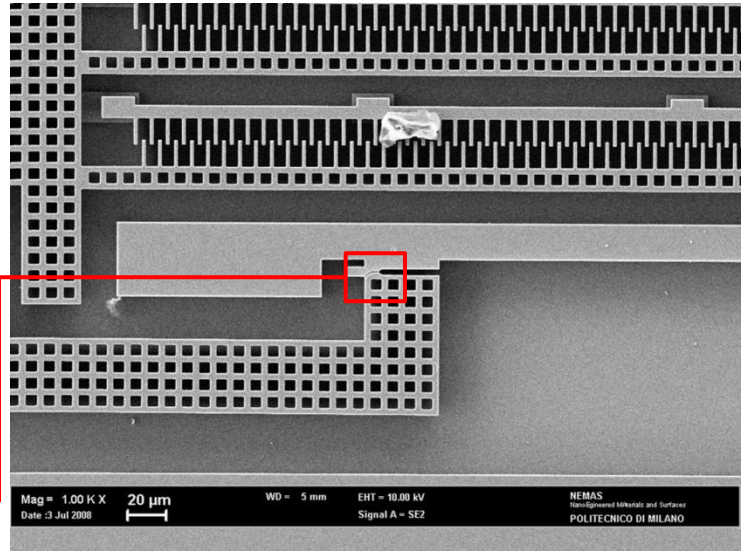

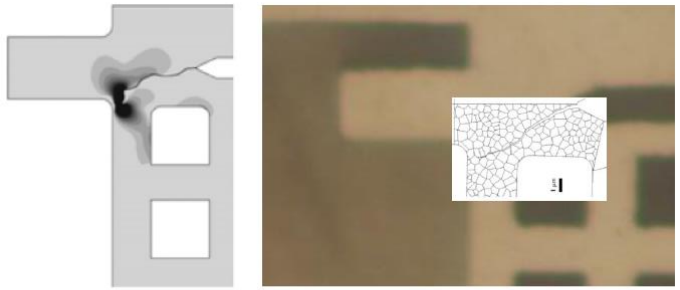

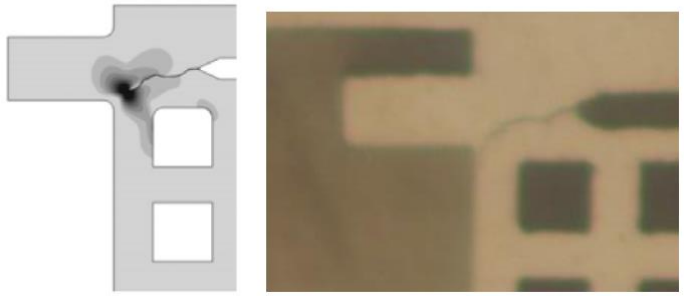

Full coupling of meso- and micro-scale analyses: a proposal based on Partition of Unity (X-FEM)

Former proposal of a test-structure to measure polysilicon toughness (on-chip test)

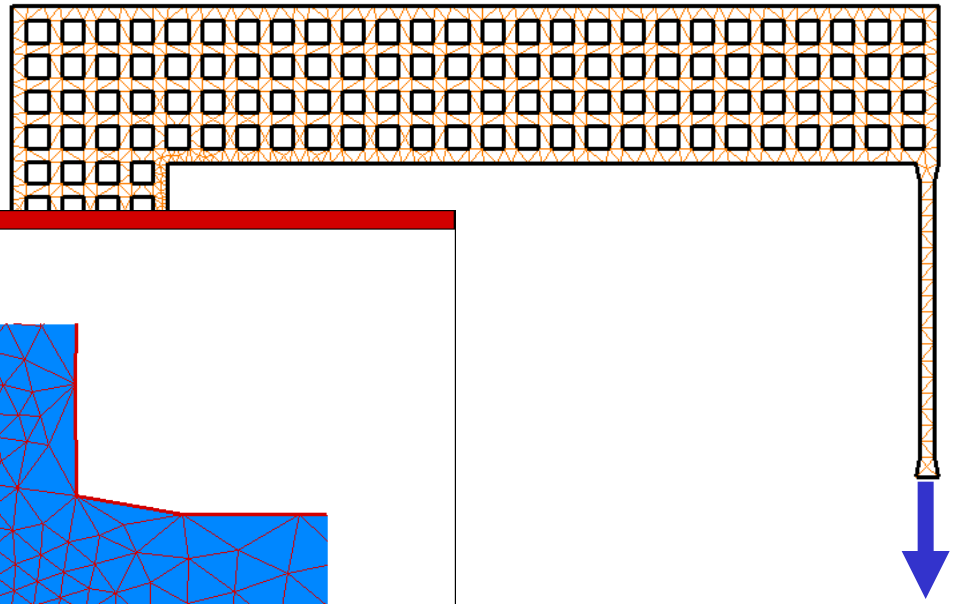

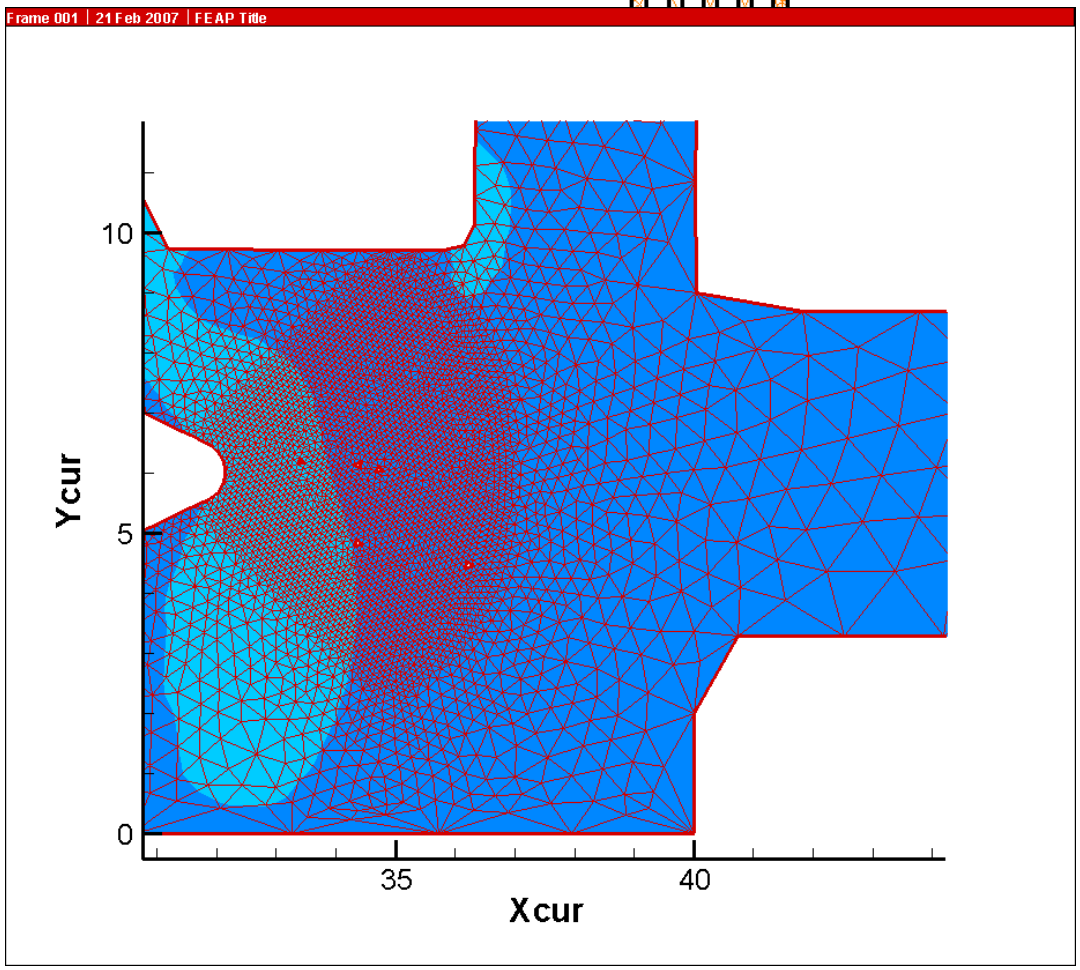

Mesh layout does not depend on crystal topology

Monte-Carlo simulations by changing the crystal morphology without modifying FE mesh

Micro-scale analysis:
3D forecast of crack pattern at failure close to anchor

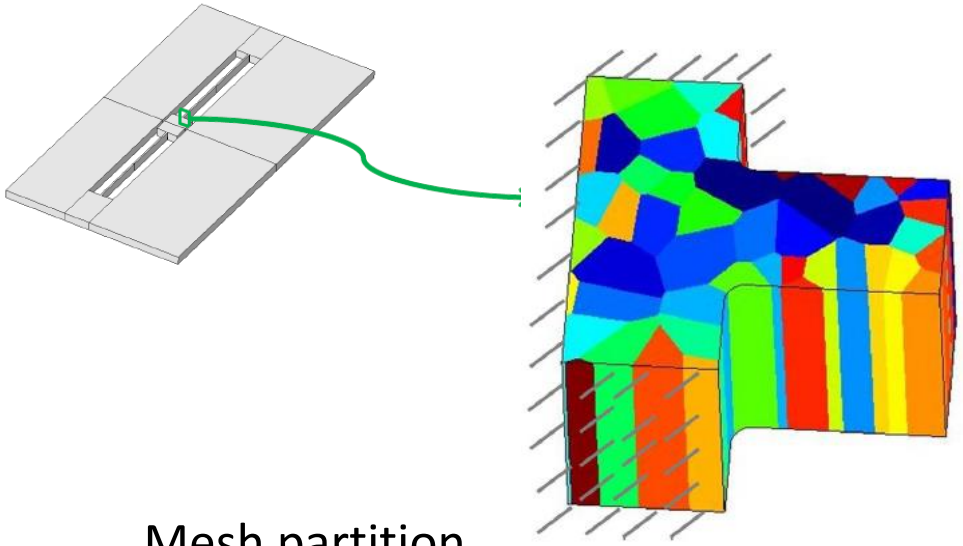

FE mesh	
Number of elements	142,648 quad tetra
Number of nodes	202,286
DOFs	**606,858**

Mesh partition into subdomains

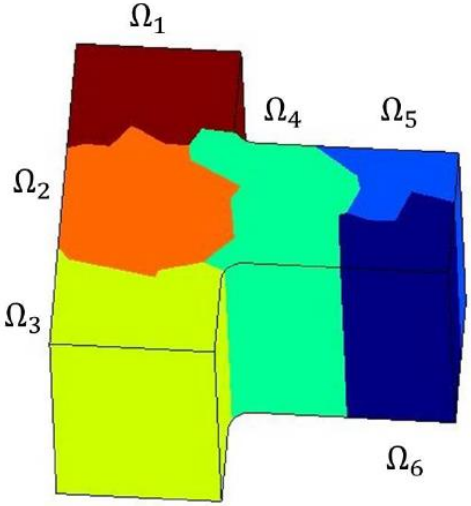

FE mesh

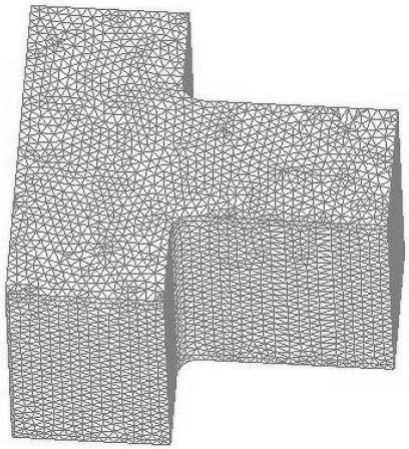

crack pattern at failure

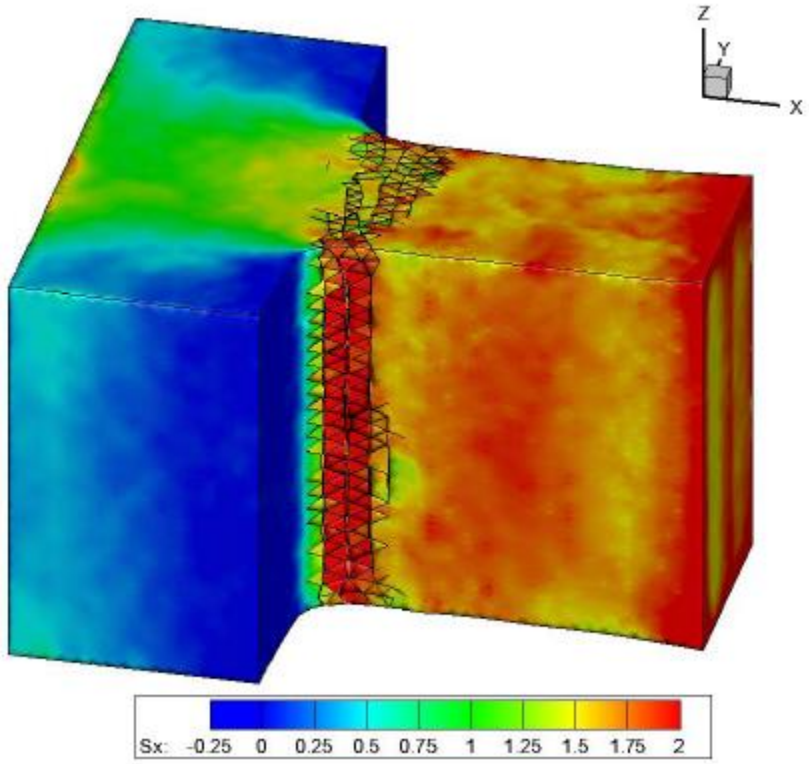

Reduced-order, multi-physics modeling and optimization

Domain Decomposition (DD) and Model Order Reduction (MOR) for coupled problems

DD and MOR for **electro-mechanical problems**

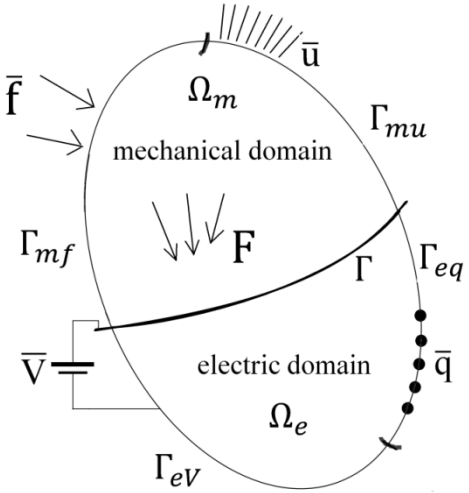

+

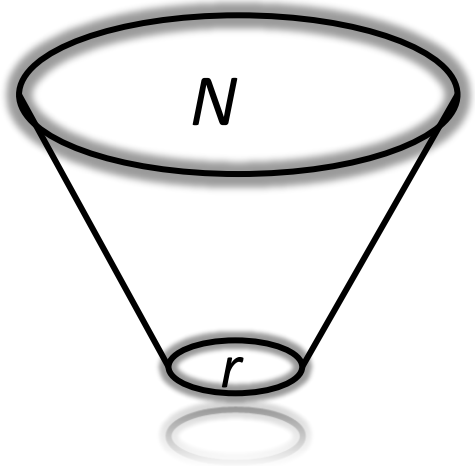

$r \ll N$

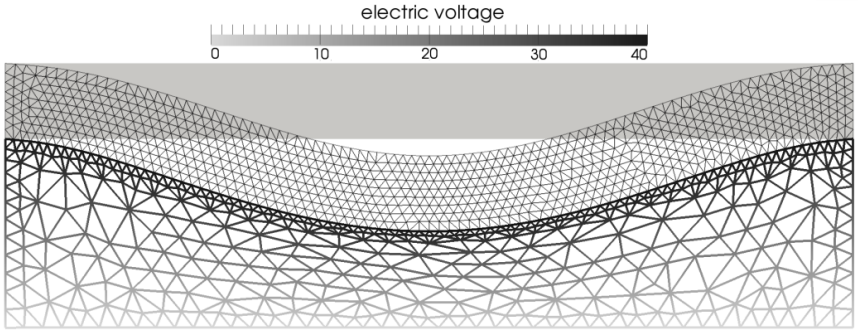

Reference problem: electro-mechanical coupling

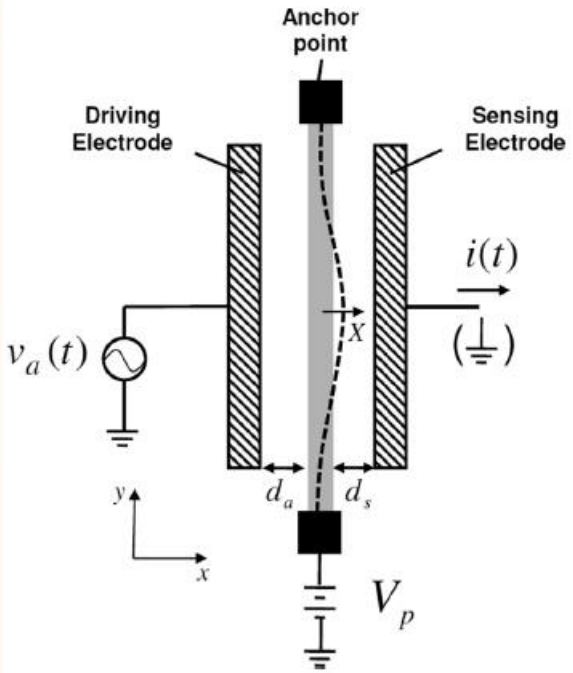

- the voltage difference (V) between the fixed and deformable electrodes cause the **charges** to **accumulate** on the surfaces between the electrical and the mechanical domains
- **electrostatic forces** on the mechanical surface cause the deformation of the structure
- the deformation of the structure causes the shape **variation of the electrostatic domain**
- **non-linear coupling** between the mechanical and the electrostatic fields

DD technique for electro-mechanical problems

Semi-discretized electro-mechanical coupled problem

$$\begin{cases} \mathbf{M}\ddot{\mathbf{U}} + \mathbf{K}_m\mathbf{U} = \mathbf{F}_{ext} + \boldsymbol{F}_{elec}(\mathrm{U}_\Gamma, \Phi) & on\ \Omega_m \\ \mathbf{K}_\phi(\mathbf{U}_\Gamma)\boldsymbol{\Phi} = \mathbf{Q}(\mathbf{U}_\Gamma, \boldsymbol{\Phi}) & on\ \Omega_e \end{cases}$$

Electric boundary condition

Mechanical boundary condition

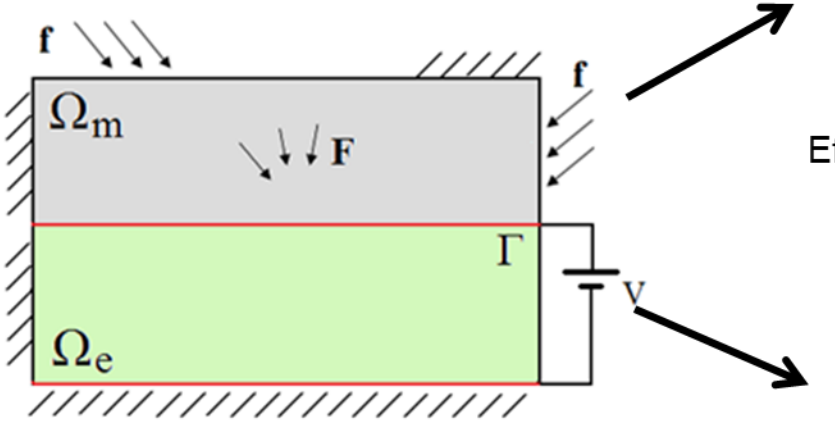

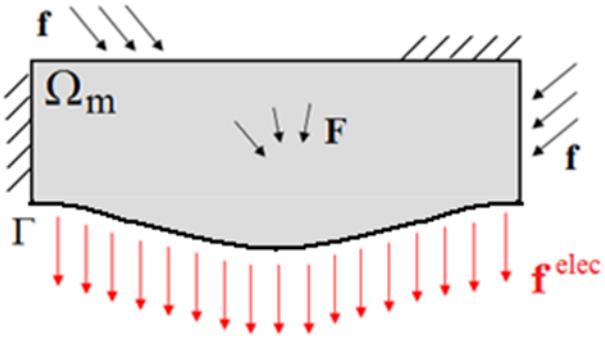

Effect of the electrostatic domain on the mechanical part: **Coulomb forces**

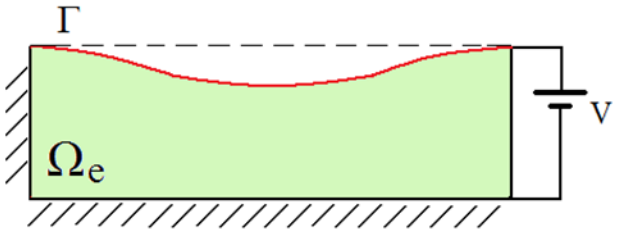

Effect of the mechanical domain on the electrical part: **change of the shape of the electrical domain**

$\mathbf{U}$ displacements of the nodes of the mechanical domain

$\mathbf{U}_\Gamma$ displacement at the interface Γ

DD technique for electro-mechanical problems

Domain decomposition approach:
- each physical field can be viewed as a sub-domain
- the solution of each physic is interpreted in an additive way

Mechanical domain:

$$\mathbf{U} = \mathbf{U}^{free} + \mathbf{U}^{link}$$

Electrostatic domain:

$$\mathbf{\Phi} = \mathbf{\Phi}^{free} + \mathbf{\Phi}^{link}$$

Free problems:

Each physics is solved indipendently

+ +

Link problems:

The physics are recoupled

Proper orthogonal decomposition (POD)-based MOR technique for electro-mechanical problems

To drastically **reduce the computational burden** of the mechanical system in the *s-th* sub-domain ($s = 1,2,\cdots,n_{sub-domains}$) of the coupled electro-mechanical problem:

Model Order Reduction via Proper Orthogonal Decomposition (POD) technique

Mechanical displacement field in the sub-domain *s*:

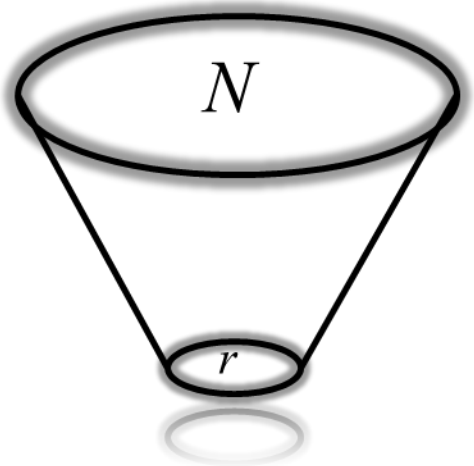

$$\mathbf{U}_s = \sum_{i=1}^{N_s} \boldsymbol{\alpha}_{i_s} \boldsymbol{\Xi}_{i_s}$$

Linear combination of orthonormal basis

$$r_s \ll N_s$$

$$\mathbf{U}_{r_s} = \sum_{i=1}^{r_s} \boldsymbol{\alpha}_{i_s} \boldsymbol{\Xi}_{i_s} = \mathbf{A}_{r_s} \boldsymbol{\Xi}_{r_s}$$

Reduced representation *of the system*

Minimization of the discrepancy between the full and the reduced representation

$$min \left\| \mathbf{U}_{r_s} - \mathbf{U}_s \right\|$$

$$\mathbf{M}_{r_s} \ddot{\boldsymbol{\Xi}}_{r_s} + \mathbf{K}_{\mathrm{m}_{r_s}} \boldsymbol{\Xi}_{\mathrm{r_s}} = \mathbf{F}_{r_s}^{ext} + \mathbf{F}_{r_s}^{elec}$$

Reduced mechanical system

Example: plane resonator

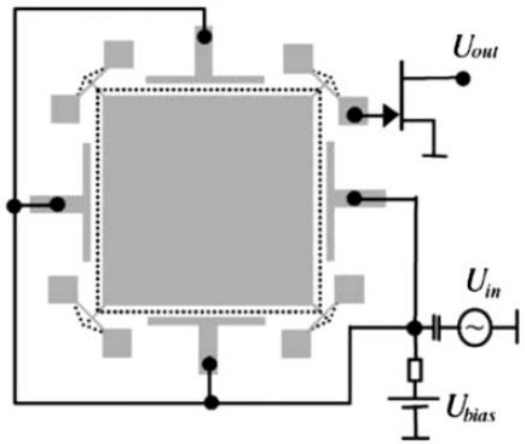

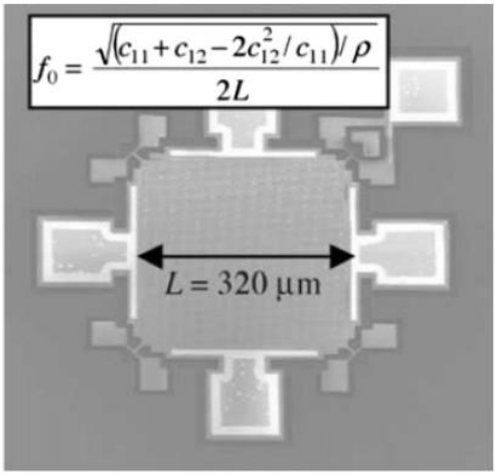

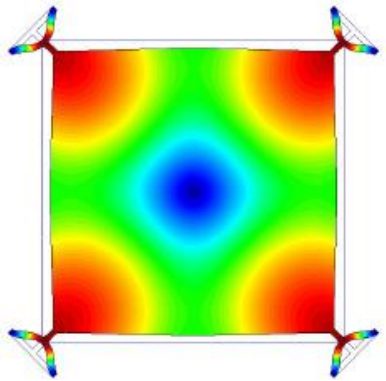

Kaajakari et al., IEEE Electr Device 2004

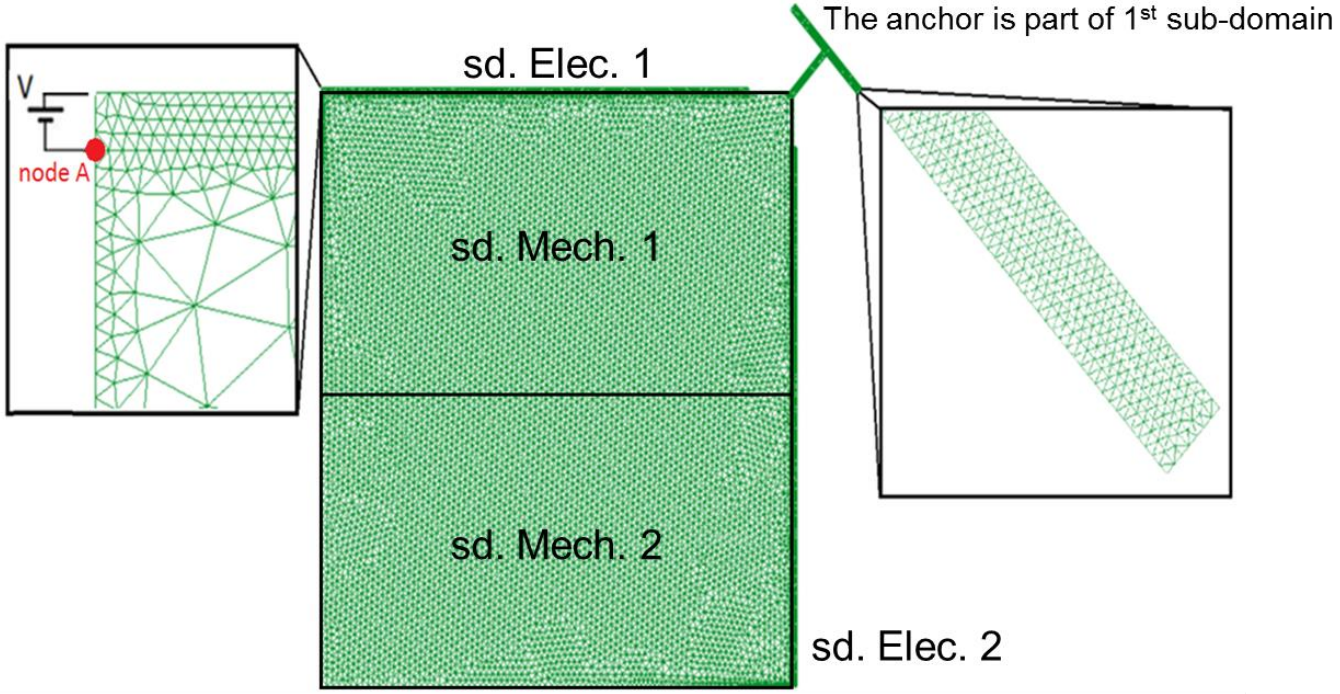

Example: plane resonator

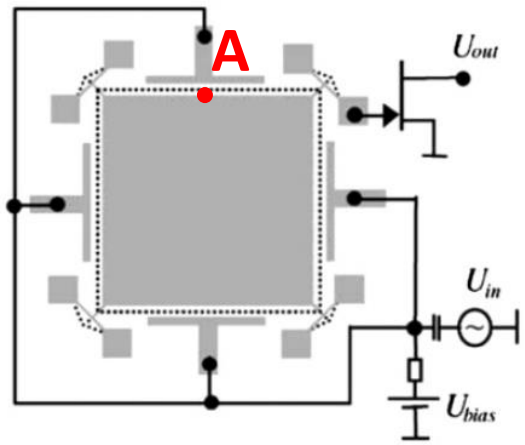

Vertical displacement of node A

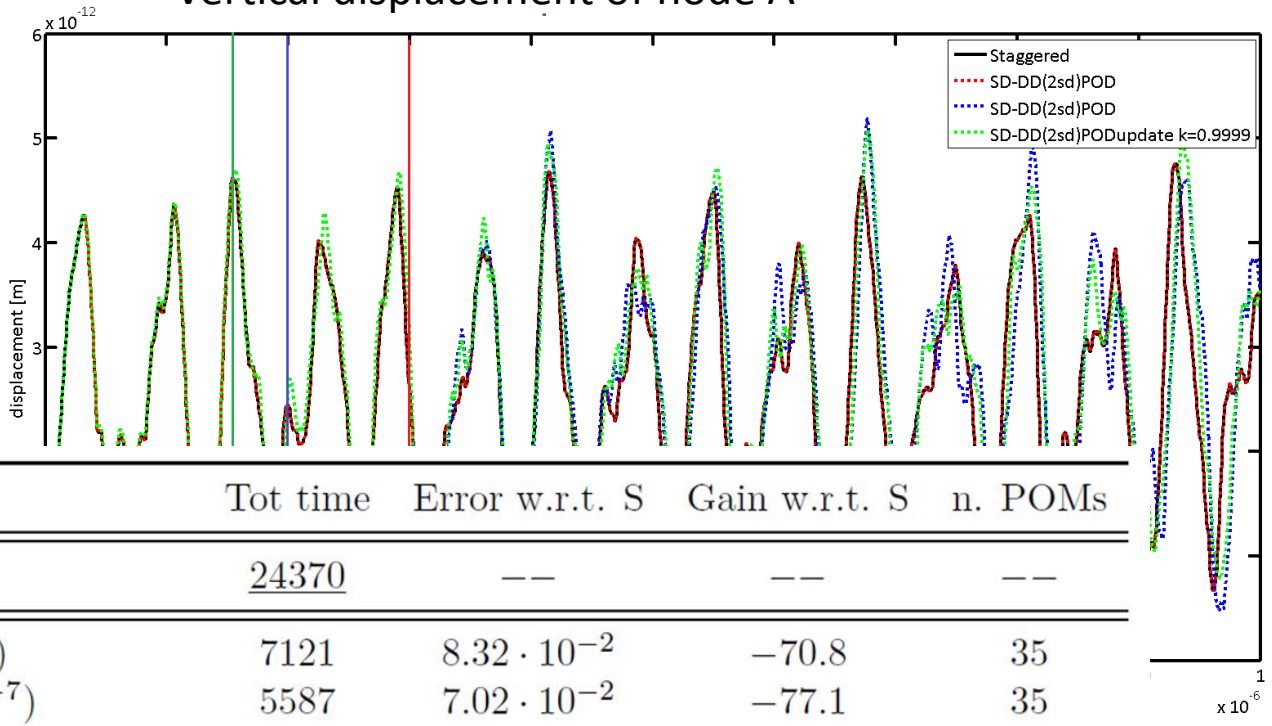

	Tot time	Error w.r.t. S	Gain w.r.t. S	n. POMs
S ($t_{tot} = 10^{-6}$)	24370	--	--	--
S-POD ($t_{snap} = 3 \cdot 10^{-7}$)	7121	$8.32 \cdot 10^{-2}$	-70.8	35
SD-POD ($t_{snap} = 3 \cdot 10^{-7}$)	5587	$7.02 \cdot 10^{-2}$	-77.1	35
S-POD ($t_{snap} = 2 \cdot 10^{-7}$)	4705	$8.33 \cdot 10^{-2}$	-80.7	38
SD-POD ($t_{snap} = 2 \cdot 10^{-7}$)	3793	$8.32 \cdot 10^{-2}$	-84.4	38
S-POD ($t_{snap} = 1.5 \cdot 10^{-7}$)	3639	$7.25 \cdot 10^{-2}$	-85.1	34
SD-POD ($t_{snap} = 1.5 \cdot 10^{-7}$)	2826	$5.86 \cdot 10^{-2}$	-88.4	34
SD-PODupdated	2664	$9.98 \cdot 10^{-2}$	-89.1	31
SD-DD(2sd)POD ($t_{snap} = 3 \cdot 10^{-7}$)	5098	$2.19 \cdot 10^{-1}$	-79	40|41
SD-DD(2sd)POD ($t_{snap} = 2 \cdot 10^{-7}$)	3670	$2.49 \cdot 10^{-1}$	-84.9	31|31
SD-DD(2sd)PODupdated	3098	$2.05 \cdot 10^{-1}$	-87.2	31|31

Multi-physics optimization of a resonant MEMS magnetometer

To have a balanced behavior

↑ **Mechanical sensitivity** $\varphi_s = \frac{2\varepsilon_0 b L_s \mathcal{V}_{\max}}{g^2}$

↑ **Bandwidth** $\varphi_b = \frac{f_{ns}}{2Q_s}$

↓ **Power consumption** $p \propto \frac{L}{bh}$

↓ **Brownian noise limited resolution** $\varphi_r = \frac{\sqrt{\frac{4k_b T K_{ms}}{2\pi f_{nms} Q_s}}}{l_{es} i}$

Process limits

(Mimimum length, etc)

Working frequency 20 kHz

For being above acoustic frequencies

Topology/structural optimization achieved through the method of moving asymptotes (MMA) by varying L, h, L_s, h_s

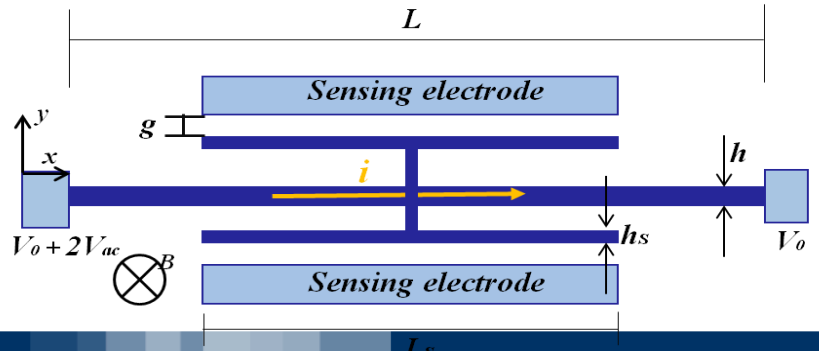

Ongoing activities

3D modeling of crack initiation and propagation:

- adaptive partitioning (domain decomposition, DD) during crack growth
- simultaneous handling of implicit/explicit time integration techniques
- parallel implementation
- multi-physics (thermo-electro-magneto-mechanical) reduced order modeling through POD (proper orthogonal decomposition)
- structural/topology optimization

Acknowledgments

- ENIAC project "*Lab4MEMS II Micro-Optical MEMS, micro-mirrors and pico-projectors*"
- Italian MIUR-PRIN projects "*Mechanics of microstructured materials: multi-scale identification, optimization and active control*" and *"Multi-scale, multi-physics and domain decomposition methods in the mechanics of microsystems and nano and micro-structured materials"*
- Regione Lombardia and CILEA-CINECA Consortium projects "*M^2-MEMS"* and *"POLYFRAC"*
- Fondazione Cariplo project